LMSC-D057194

UNSTEADY AERODYNAMIC FLOW FIELD ANALYSIS OF THE SPACE SHUTTLE CONFIGURATION

Part III: UNSTEADY AERODYNAMICS OF BODIES WITH CONCAVE NOSE GEOMETRIES

by
Lars E. Ericsson and J. Peter Reding
April 1976

Prepared Under Contract NAS 8-30652
for
National Aeronautics and Space Administration

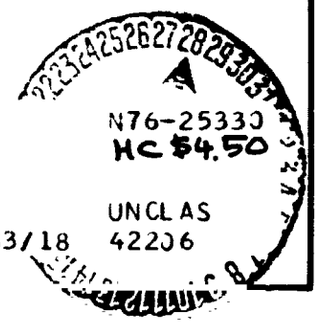

Lockheed MISSILES and SPACE COMPANY, INC.
SUNNYVALE, CALIFORNIA

UNSTEADY AERODYNAMIC FLOW FIELD ANALYSIS OF THE SPACE SHUTTLE CONFIGURATION

Part III: UNSTEADY AERODYNAMICS OF BODIES WITH CONCAVE NOSE GEOMETRIES

by

Lars E. Ericsson and J. Peter Reding

April 19[illegible]

Prepared Under Contract NAS 8-30652

for

National Aeronautics and Space Administration

Lockheed Missiles & Space Company, Inc.
A Subsidiary of Lockheed Aircraft Corporation
Sunnyvale, California

ABSTRACT

An analysis of the unsteady aerodynamics of bodies with concave nose geometrics has been performed. The results show that the experimentally observed pulsating flow on spiked bodies and in forward facing cavities can be described by the developed simple mathematic model of the phenomenon.

Static experimental data is used as a basis for determination of the oscillatory frequency of spike-induced flow pulsations. The agreement between predicted and measured reduced frequencies is in general very good. The spiked-body mathematical model is extended to describe also the pulsations observed in forward facing cavities and it is shown that not only can the frequency be predicted but also the pressure time history of the pulsation phenomenon can be described with the accuracy needed to predict the experimentally observed time average effects. This implies that it should be possible to determine analytically what the impact of the flow pulsation is on the structural integrity of the nozzles on the jettisoned empty SRM-shells.

CONTENTS

PRECEDING PAGE BLANK NOT FILMED

ILLUSTRATIONS

Figure

ILLUSTRATIONS (Continued)

Figure

Section 1
INTRODUCTION

According to present plans the Solid Rocket Motors (SRM's) of the space shuttle launch vehicle are to be jettisoned after burnout and recovered for renewed usage (Ref. 1). Consequently, wind tunnel tests have been made of the SRM's in the complete angle of attack range $0 \leq \alpha \leq 180°$ (Ref. 2). Recent tests (Ref. 3) showed that the SRM could have a stable trim point when it was "flying backward" at supersonic speed, and that discontinuous changes of the aerodynamic characteristics occur in that α-range, $140° < \alpha < 180°$ (Fig. 1). The discontinuous flow change is associated with α-hysteresis and pulsating unsteady flow (Fig. 2), all characteristics that have been observed on spiked bodies. Consequently, the spiked body analysis performed earlier, when determining the effect of the escape rocket on the Apollo-Saturn launch vehicles (Refs. 4-7), has been reexamined. New analytic methods have been developed which can predict the frequency at which large scale spike-induced oscillatory or pulsatory flow occurs. This analytic tool has been applied, after some modification, to obtain an assessment of the frequency at which flow pulsations occur on forward facing cavities, e.g., the SRM-rocket nozzle. A simple formulation of the pressure time history during one pulsation cycle has also been suggested which provides time average results that agree well with the experimentally observed discontinuous changes in the static aerodynamic characteristics of the SRM rockets.

Section 2
DISCUSSION

Kabelitz (Refs. 8 and 9) has performed a thorough theoretical and experimental investigation of the unsteady flow on biconic concave nose geometries. He shows how, when the spike is lengthened, the pulsating flow phenomenon (Fig. 3a) is transformed to another unsteady flow geometry (Fig. 3b), which he calls "oscillations" and Album (Ref. 10) has referred to as "flexions." Kabelitz also discusses a third form of flow unsteadiness, "vibrations," which occur when the spike is lengthened further (Fig. 4).

2.1 Causes of Flow Unsteadiness

Maull (Ref. 11) explained the pulsating flow occurrence in the following simple manner. When the external flow U_e can be turned by an attached conical shock, a steady flow condition exists (see top half of Fig. 5). Maull computed the largest spike length that would allow this attached conic shock for various shoulder radii on the flat cylinder face. He found that this critical geometry agreed rather well with the experimentally established boundary between stable and pulsatory flow (Fig. 6). When the required flow turning angle is larger than what can be accomplished by such an attached conical shock, a detached strong shock is formed which causes most of the shear layer to be turned back into the recirculatory region (see bottom half of Fig. 5). As a result the recirculatory region starts to grow and the pulsating flow is established.

It may seem overly simplistic to use this purely inviscid flow concept to determine when a viscous flow phenomenon starts. However, Elfstrom (Ref. 12) has used the same concept to determine when incipient separation starts in high Reynolds number flow; it starts when the required flow turning angle exceeds that allowing an attached oblique or conic shock. Bogdonoff et al (Ref. 13) show that Elfstrom's simple inviscid concept agrees better with experimental data than other more involved

mathematical models (e.g., Ref. 14). The same simple inviscid flow concept also predicts when shock-induced separation will occur on a delta wing at supersonic speeds; it occurs when the leading edge shock becomes detached, thereby creating an embedded supersonic flow region, that is terminated by a normal shock, which usually will be strong enough to cause the boundary layer to separate (Refs. 15-17).

Kabelitz (Ref. 8) speculates that the reasoning behind Maull's criterion for flow unsteadiness was that the flow aft of the reattachment shock(s) (aft of WE in Fig. 6) goes subsonic, which of course almost coincides with the shock detachment event (Ref. 18). Kabelitz (Ref. 8) has himself performed a more elaborate analysis. The stationary closed separated flow domain is assumed known, defined by available experimental data. The stability boundaries for this closed separated flow region are determined using a linear perturbation analysis in which the "unknowns" are lumped into one global damping parameter (λ_U). It is shown that the boundary between oscillatory and pulsating flow is rather insensitive to the value of this parameter λ_U, and that the predicted boundary agrees well with that determined experimentally[#]. However, the boundary between stable and oscillatory flow cannot be determined because it is very much dependent on the unknown value of the damping parameter λ_U.

2.2 Determination of Oscillation Period

Frames b through f in Figure 3a show how the recirculatory region grows as a result of the free shear layer being turned back into the recirculatory region by the strong (reattachment) shock. When the front of this growing separated flow region reaches the spike tip the separation region collapses and is "spilled" downstream over the cylinder shoulder in the form of a ring vortex (Ref. 19). The recirculatory flow build-up then starts all over again as is shown in frame a of Figure 3a. Thus, the time period for one cycle of pulsation is composed as follows.

$$T = L_S/U_\infty + L_S/\bar{U}_u \qquad (1)$$

[#]The analysis is limited to pointed, concave, biconic forebodies.

$\bar{U}_u$ is the mean upstream convection velocity of the mass flow added to the recirculatory region by the strong reattachment shock interaction. After reaching the spike tip the separated flow region is "spilled" downstream with the free stream velocity.

The Strouhal number defined by Eq. (1) is

$$S_{L_S} = \frac{f\, L_S}{U_\infty} = \left[1 + \frac{U_\infty}{\bar{U}}\right]^{-1} \tag{2}$$

The approach used earlier in the analysis of spike-induced unsteady aerodynamics (Refs. 4-6) will be used to determine the convection velocity $\bar{U}_u$. Thus, how $\bar{U}_u$ varies with spike length is going to be determined through the spike efficiency as a forebody drag reducer.

The stable and unstable flow conditions for a critical spike geometry (the crosses and circles in Fig. 6) are illustrated in the top and bottom halves, respectively, of Figure 5. Thus, the overflow mass flow being turned back in the unstable case is transported upstream with the steady state convection velocity, U_{uc}, existing at an earlier time instant. It is assumed that the velocity $\bar{U}_u$ in Eq. (2) is proportional to the mean convection velocity, $\bar{U}_{uc}$, for the corresponding fictitious steady flow condition[#]. This steady state convection velocity $\bar{U}_{uc}$ will decrease with decreasing spike length since the back-flow-driving pressure rise through the reattachment shock is decreasing (Fig. 8). In Figure 9 the hypothetical steady state flow case is represented in idealized form. It is assumed that for the spike lengths of interest the flow profiles in the top half of Figure 9 remain similar. An equivalent flow geometry, from drag reduction standpoint, is sketched in the bottom half of Figure 9. Using it the maximum drag reduction, obtained with the longest spike that will retain flow separation from the spike tip, can be expressed as follows:

$$\left(\Delta C_{A_o}\right)_{MAX} \sim \left(\bar{D}_o\right)^2_{MAX} U_\infty{}^2 \tag{3}$$

[#]Kabelitz (Ref. 8) has shown that application of steady flow parameters to the unsteady flow works well.

Neglecting density variations between different flow profiles the drag reduction for a less than optimum spike length can be written

$$\Delta C_{A_o} \sim \left(\bar{D}_o\right)^2_{MAX} \bar{U}^2 \tag{4}$$

This is due to the fact that the flow reattachment on the cylinder face remains at the same near-shoulder location also for the shorter spike.

According to the assumption of similar flow profiles the following holds for real and idealized flow geometrics.

$$\left.\begin{aligned} \left(U_{uc}\right)_{MAX} \Big/ \left(U_e\right)_{MAX} &= U_{uc}/U_e \\ \left(\bar{U}_{uc}\right)_{MAX} \Big/ U_\infty &= \bar{U}_{uc}/\bar{U} \end{aligned}\right\} \tag{5}$$

Eqs. (3) and (5) give the following definition of $\bar{U}/U_\infty$

$$\bar{U}/U_\infty = \left[\Delta C_{A_o} \Big/ \left(\Delta C_{A_o}\right)_{MAX}\right]^{1/2} \tag{6}$$

With $\bar{U}_u \sim \bar{U}_{uc}$ Eqs. (5) and (6) give

$$\bar{U}_u \Big/ \left(\bar{U}_u\right)_{MAX} = \bar{U}/U_\infty = \left[\Delta C_{A_o} \Big/ \left(\Delta C_{A_o}\right)_{MAX}\right]^{1/2} \tag{7}$$

Finally, combining Eqs. (2) and (7) gives

$$\left.\begin{aligned} \frac{S_{LS}}{\left(S_{LS}\right)_{OPT}} = \left[\frac{\Delta C_{Ao}}{\left(\Delta C_{Ao}\right)_{MAX}}\right]^{1/2} \Bigg\{ & 1 \\ & + \frac{\left(\bar{U}_u\right)_{MAX}}{U_\infty} \left[1 - \frac{\bar{U}_u}{\left(\bar{U}_u\right)_{MAX}}\right] \Bigg\} \end{aligned}\right\} \tag{8}$$

In order to obtain information about $\Delta C_{Ao}/(\Delta C_{Ao})_{MAX}$ one has to study geometrics that allow steady flow for the (L_S/D) - range of interest#. Spiked bodies with rounded (e.g., spherical) shoulders form one such family (Ref. 10). From an earlier study (Refs. 5-7) the results shown in Figures 10 and 11 were obtained. Using the linear representation in Figure 11 one can write Eq. (8) as follows:

$$\frac{S_{LS}^*}{S_{LS}} = \frac{(S_{LS})_{OPT}}{S_{LS}} \sim \left[\left(\frac{\bar{L}}{\bar{D}} \right)_{OPT} \Big/ \left(\frac{\bar{L}}{\bar{D}} - \frac{\Delta_{sh}}{\bar{D}} \right) \right]^{1/2} \tag{9}$$

For flat-faced bodies with thin pointed spikes $\bar{L}/\bar{D}$ can be substituted with L_s/D. Pulsating flow data for such bodies (Refs. 20 and 21) give the results shown in Figure 12. The data have been normalized to the reattachment conditions for the optimum spike length using Eq. (9). The data are seen to scatter around a straight line. The decrease of S_{LS}^* with increasing $(L_S/D - \Delta_{sh}/D)$ reflects the fact that the second term within the "arrow-bracket" in Eq. (8) decreases as $\bar{U}_u/\bar{U}_{u\ MAX}$ increases with increasing spike length. The results in Figure 12 together with Eq. (9) define S_{LS} as follows:

$$S_{LS} = \frac{0.32}{(L_S/D)_{OPT}^{1/2}} \left[\frac{L_S}{D} - \frac{\Delta_{sh}}{D} \right]^{1/2} \left[1 - 0.14 \left(\frac{L_S}{D} - \frac{\Delta_{sh}}{D} \right) \right] \tag{10}$$

The experimental results in Figure 10 can be approximated as follows:

$$\left(\frac{\bar{L}}{\bar{D}} \right)_{OPT} = \left(\frac{L_S}{D} \right)_{OPT} = \begin{cases} 1.6\ (1 + 0.1\ M_\infty) & :\ M_\infty \leq 11.3 \\ 3.4 & :\ M_\infty > 11.3 \end{cases} \tag{11}$$

For the bluff geometrics producing pulsating flow a good approximation of the (no spike) shock detachment distance is the following (Ref. 22).

$$\frac{\Delta_{sh}}{D} = 0.515 \Big/ \left(\frac{\hat{\rho}}{\rho_\infty} - 1 \right)^{1/2} \tag{12}$$

where $\hat{\rho}/\rho_\infty$ is the density ratio through a normal shock.

#Kabelitz (Ref. 8) has shown that application of steady flow parameters to the unsteady flow works well.

Combining Eqs. (10) - (12) gives the S_{LS} - predictions shown in Figure 13 for M_∞ = 2, 4, 6, 8, 10, and ∞. The agreement with available experimental data (Refs. 11, 20, 21, 23-26) is generally very good. It is only Maull's single data point (Ref. 11) that shows any substantial deviation. The reason for this is not known. The results in Figure 13 are all for pointed thin spikes. If the spike has a blunt tip, e.g., a planar cut, the measured frequencies (Ref. 24) are higher than what is predicted by Eqs. (10) - (12)[#]. The reason for this is that the reattachment conditions are those corresponding to a longer pointed spike (see sketches in Fig. 14). In this case, and also when a "hammerheaded" spike tip is used, one needs forebody drag measurements in lieu of Eqs. (10 and (11) for the determination of S_{LS}.

It is clear that the similar profile assumption used to derive Eq. (10) is not valid for short spike lengths. When L_S/D exceeds Δ_{sh}/D the established recirculatory flow region starts out with a finite upstream convection velocity and not with $\bar{U}_u = 0$, which is the value used in Eq. (10). That is, the predicted S_{LS} - values in Figure 13 should be finite, not zero, when $(L_S/D - \Delta_{sh}/D)$ approaches zero. One way to accomplish this is to extend the predictions tangentially below a certain shock penetration.

Judging by the experimental data in Figure 13 it appears reasonable to make this linear extension for $(L_S/D - \Delta_{sh}/D) \leq 0.25$. Thus Eq. (10) is modified as follows:

$$S_{LS} = \frac{0.32}{\left(L_S/L_{/OPT}\right)^{1/2}} \begin{cases} \left(\frac{L_S}{D} - \frac{\Delta_{sh}}{D}\right)^{1/2} \left[1 - 0.14\left(\frac{L_S}{D} - \frac{\Delta_{sh}}{D}\right)\right]; & \frac{L_S}{D} - \frac{\Delta_{sh}}{D} > 0.25 \\ 0.26\left[1 + 3.46\left(\frac{L_S}{D} - \frac{\Delta_{sh}}{D}\right)\right] & ; \quad \frac{L_S}{D} - \frac{\Delta_{sh}}{D} \leq 0.25 \end{cases} \tag{13}$$

The similar flow profile assumption also breaks down at the other end of the $(L_S/D - \Delta_{sh}/D)$ - range. For deep spike penetration the reattachment conditions approach a constant value. Eq. (2) shows that for $\bar{U}_u$ = constant S_{LS} = constant.

[#]It should be noted that Maull (Ref. 11) used a pointed spike, and that no corner roundness is present for the data point shown in Fig. 13.

This constant value for large spike lengths is S_{LS}^*. Figure 11 shows that in the linear approximation $\Delta C_{Ao} = (\Delta C_{Ao})_{MAX}$ when

$$\frac{L_S}{D} - \frac{\Delta_{sh}}{D} = \frac{2}{3}\left(\frac{L_s}{D}\right)_{OPT} \tag{14}$$

Together with Eqs. (10) and (11) Eq. (14) gives

$$S_{LS}^* = 0.26 - 0.024\left(\frac{L_S}{D}\right)_{OPT} \tag{15}$$

Combining Eqs. (11) and (15) gives S_{LS}^* as a function of Mach number (Fig. 15). As this S_{LS}^* is for flat-faced cylinders, Figure 15 represents the maximum Strouhal number for all spike-induced flow pulsations. Figure 11 shows that the deviation from the linear relationship, and the associated similar flow assumption, Eq. (10), begins at

$$\frac{L_S}{D} - \frac{\Delta_{sh}}{D} = 0.45\left(\frac{L_S}{D}\right)_{OPT} \tag{16}$$

Letting S_{LS} reach S_{LS}^* in a smooth high order fasion for $L_S/D - \Delta_{sh}/D = (L_S/D)_{OPT}$ gives the following modification of Eq. (13)

$$S_{LS} = \begin{cases} \dfrac{0.0356}{X_\ell^{1/2}}\left[1 + 3.46\left(\dfrac{L_S}{D} - \dfrac{\Delta_{sh}}{D}\right)\right] & ; \ \dfrac{L_S}{D} - \dfrac{\Delta_{sh}}{D} < \dfrac{1}{4} \\ \dfrac{0.214}{X_\ell^{1/2}}\left(\dfrac{L_S}{D} - \dfrac{\Delta_{sh}}{D}\right)^{1/2}\left[1 - 0.14\left(\dfrac{L_S}{D} - \dfrac{\Delta_{sh}}{D}\right)\right] & ; \ \dfrac{1}{4} \le \dfrac{L_S}{D} - \dfrac{\Delta_{sh}}{D} \le X_\ell \\ S_{LS}^* - \left(S_{LS}^* - S_{LS_\ell}\right)\left[\dfrac{\dfrac{L_S}{D} - \dfrac{\Delta_{sh}}{D} - \left(\dfrac{L_S}{D}\right)_{OPT}}{0.55\left(\dfrac{L_S}{D}\right)_{OPT}}\right]^n & ; \ \dfrac{L_S}{D} - \dfrac{\Delta_{sh}}{D} > X_\ell \end{cases} \tag{17}$$

where

$$n = -\frac{0.059\left(\frac{L_S}{D}\right)_{OPT}\left(1 - 0.14\,X_\ell\right)}{X_\ell\left(S_{LS}^{*} - S_{LS_\ell}\right)}$$

$$X_\ell = 0.45\left(L_S/D\right)_{OPT}$$

$$S_{LS}^{*} = 0.260 - 0.0535\,X_\ell$$

$$S_{LS_\ell} = 0.214 - 0.030\,X_\ell$$

Figure 16 shows the predictions by Eq. (17) compared with the experimental data (Refs. 11, 20, 21, 23-26). As most of the experimental data fall in the region for which Eq. (10) is valid, $0.25 \leq (L_S/D - \Delta_{sh}/D) \leq 0.45\,(L_S/D)_{OPT}$, the improvement in agreement between experiment and theory is not very striking when comparing Figs. 13 and 16. If the main body face is not flat but of some convex geometry, an effective spike length $\bar{L}$ can be defined as the axial distance between spike tip and reattachment (see inset in Fig. 10). In this case the reattachment diameter $\bar{D}$ may also be significantly different from D. Thus $\bar{L}/\bar{D}$ has to be used instead of L_S/D.

2.3 Effect of Forward Facing Cavity

When the face of the main (spike-supporting) body consists of a thin-lipped forward facing cavity, the pulsating flow condition persists even for long spikes that would produce stable flow on a regular flat faced body (see Ref. 27 and Fig. 17). It is clear that the depth (h_C) of the cylindrical cavity should be included in the characteristic length when defining a Strouhal number for cavity-spike geometrics. This effective Strouhal number ($\bar{S}_{LS}$) should approach that for regular spiked bodies (S_{LS}) when the cavity depth (h_C) goes to zero, n.b. provided that pulsating flow would exist for the regular spiked-body geometry. In view of this it appears reasonable to let this union between $\bar{S}_{LS}$ and S_{LS} take place at the break-away point defined by Eq. (16).

The break-away for the regular spiked body occurred because S_{LS} was approaching an upper limit (S_{LS}^{*}) when the spike length was increased further, a limit that never is realized because the flow becomes stable before the optimum spike length is approached. For the cavity-spike geometry the break-away will be in the opposite

direction. As more and more mass flow is captured by the sharp cavity rim with increasing spike length, $\bar{U}_u$ in Eq. (2) continues to increase[#]. If one assumes that this increase occurs in a (locally) linear fashion the break-away takes the simple tangential form and Eq. (13) is modified as follows:

$$\bar{S}_{LS} = \frac{0.32}{(L_S/D)^{1/2}_{OPT}} \begin{cases} 0.26\left[1 + 3.46\left(\frac{L_S}{D} + \frac{h_C}{D} - \frac{\Delta_{sh}}{D}\right)\right] & ; \\ \quad \frac{L_S}{D} + \frac{h_C}{D} - \frac{\Delta_{sh}}{D} \le \frac{1}{4} & \\ \left(\frac{L_S}{D} + \frac{h_C}{D} - \frac{\Delta_{sh}}{D}\right)^{1/2}\left[1 - 0.14\left(\frac{L_S}{D} + \frac{h_C}{D} - \frac{\Delta_{sh}}{D}\right)\right] & ; \\ \quad \frac{1}{4} < \frac{L_S}{D} + \frac{h_C}{D} - \frac{\Delta_{sh}}{D} < X_\ell & \\ \frac{1}{2}\left[X_\ell^{1/2}(1 + 0.14\,X_\ell) + \frac{1 - 0.42\,X_\ell}{X_\ell^{1/2}}\left(\frac{L_S}{D} + \frac{h_C}{D} - \frac{\Delta_{sh}}{D}\right)\right]; & \\ \quad \frac{L_S}{D} + \frac{h_C}{D} - \frac{\Delta_{sh}}{D} \ge X_\ell & \end{cases}$$

where $X_\ell = 0.45\,(L_S/D)_{OPT}$ (18)

Figure 17 shows that the predictions through Eq. (18) are in good agreement with the experimental results obtained by Hermach et al (Ref. 27). Also shown in Figure 17 is one data point for the empty SRM shell "flying backwards." In what follows it will be explained how this data point was introduced into the graph of Figure 17.

Johnson (Ref. 28) has performed tests at high Mach numbers, $M_\infty > 21.6$, of an unspiked forward facing cylindrical cavity. He shows that the flow is stable and the shock configuration can not be distinguished from that of a flat faced cylinder. This is for $\alpha = 0$ and no mass addition into the cavity. When mass addition is provided through an orifice in the center of the cavity bottom, this "fluid spike" starts a pulsating flow phenomenon. In difference to that observed by Hermach et al on the

[#]Provided that the cavity depth is fully effective, i.e., for $h_C/D < 1$.

spiked cavity (Ref. 27), this pulsating flow phenomenon is asymmetric and nonperiodic. Johnson describes it as follows: "shock bulges out on one side but the asymmetry rotates." The statement about non-periodicity should be judged against the fact that only high-speed motion pictures were used to arrive to this conclusion. Demetriades (Ref. 26) has observed a similar asymmetric pulsating flow phenomenon on a stubby, tension-shell-like, spiked body. He finds, using fluctuating pressure data, that also this rotating-pulsating flow phenomenon definitely is periodic.

When Johnson (Ref. 28) changed the cavity geometry to a conical shape, the flow again was steady without mass addition but became unsteady when the "fluid spike" was present. In this case, however, the asymmetric flow phenomenon does not rotate. Johnson's description is: "part of the shock is fixed, extending into the cavity; other part of shock snaps in and out." These same words also describe what one sees in the flow photographs for the pulsating flow phenomenon on the SRM nozzle in Figure 2, and on the hollow skirt of a Polaris re-entry body in Figure 18 (Ref. 29). In these latter cases the asymmetric flow pulsation is started when at a certain flow inclination the windward branch of the bow shock jumps inside the conic cavity (see Figs. 2 and 18). The sketch in Figure 19 illustrates how this flow pulsation at non-zero angle of attack (Fig. 19a) is the "asymmetric equivalent" to the pulsating flow existing at $\alpha = 0$ for a spiked cavity (Fig. 19b). The sketches show the hypothetical unstable reattachment conditions starting the pulsating flow.

In the case of the spiked cavity the most forward extent of the pulsating separated flow region is determined by the spike tip. This is also true for a regular spiked body, in which case the smallest forward extent is obtained when the spike just penetrates the no-spike bow shock, i.e., $L_S \geq \Delta_{sh}$ for pulsating flow. Figure 2 shows that the distance between the most forward and aft positions of the pulsating strong shock (with associated separated flow region) is approximately equal to the shock detachment distance for stable flow at $\alpha = 0$. It therefore seems reasonable to assume that the "effective spike length" is $L_S = k\,\Delta_{sh}$. The results in Figure 2 give $k = 1$, and for lack of more extensive test results this value will be used in the present

analysis.* Thus, the SRM-nozzle data point in Figure 17 was obtained from the measured Strouhal number $(S_D)_{SRM} = 0.18$, based on the SRM-diameter, by converting it to an effective spike Strouhal number S_{LS} through the following relationship.

$$\bar{S}_{LS} = (S_D)_{SRM} \frac{D_I}{D_{SRM}} \left(\frac{h_C}{D_I} + \frac{\Delta_{sh}}{D} \frac{D_E}{D_I} \right) \tag{19}$$

Δ_{sh}/D is obtained from Eq. (12). D_I is the mean## internal nozzle diameter and D_E is the maximum external body diameter in the exit plane (i.e., including skirt).

2.4 Control of Pulsating Flow

It may be desirable to change the frequency of the flow pulsations to avoid resonance with a structural frequency. How this can be done by changing spike and/or cavity geometry is shown by the analytic formulas developed earlier in subsections 2.2 and 2.3. If the change is large enough the more dangerous pulsating flow phenomenon transforms into oscillations or possible to steady flow* (see Fig. 4). Rounding the face shoulder (Ref. 11) or decreasing the cone angle from $\theta_N = 90°$ (Ref. 8) are effective means for stopping the flow pulsations. When these straightforward control measures do not suffice, one has to use more sophisticated means. Obviously the reattachment process and associated unstable flow phenomena are very much dependent upon the character of the impinging free shear layer. If the shear layer profile is stretched, the reattachment conditions at the shoulder of a spiked body may approach those for a small protuberance in a thick boundary layer (Refs. 30 - 32). Such a change of the free shear layer profile is obtained by increasing the Mach number and/or decreasing the air density.

*Although k should be dependent on at what α' the pulsations occur, the α'-range seems to be limited to $35° < \alpha' < 45°$ (Figs. 1 and 2), and a k-value independent of α' can be used.

##Volume wise, that is. It is the diameter marked D in Fig. 17.

*Kabelitz' vibrations are included in the "steady flow" nomenclature used in the present report.

Figure 20 shows how the reattachment configuration on a flow separation disk undergoes this type of shear layer thickening when the Mach number is increased above $M_\infty = 5$ (Ref. 5). The absence of the strong reattachment shocks at the disk rim for $M_\infty > 5$ signifies a loss of the discontinuous or highly nonlinear disk loading which causes dynamic instability[#] at $M_\infty < 5$. Reeves (Ref. 33) has determined the critical shear layer thickness for this change from stable to pulsating spike-induced separated flow using the experimental results obtained by Maull, Mair, and Wood (Refs. 11, 23, and 34 respectively). (See Fig. 21). The results obtained by Maull and Wood are for laminar flow, and for $L_S/D \approx 2.3$. Thus, δ_{SL}/D in Figure 21 is in that case a measure of the vorticity of the laminar shear layer at reattachment. If one considers the spiked-body flow as a special case of cavity flow, one would expect the shear layer to have a two-dimensional character. That is, it should increase as $x^{1/2}$, just as the laminar boundary layer. The laminar boundary layer thickness on a cone varies with edge Mach number as follows (Ref. 35).

$$\delta(M_e) = \delta(0)\left[1 + K_c M_e^2\right] \tag{20}$$

which suggests that

$$\frac{\delta_{SL}(M_e)}{D} = \frac{\delta_{SL}(0)}{D}\left[1 + K_{SL} M_e^2\right] \tag{21}$$

For the solid line curve shown in Figure 21 $\delta_{SL}(0)/D = 0.0165$ and $K_{SL} = 0.11$. Thus, Figure 21 indicates that for $L_S/D = 2.3$ and $\theta_N = 90°$ the critical value of the shear layer vorticity is independent of free stream Mach number.[##] The corresponding critical shear layer edge Reynolds number at reattachment is

$$\left(Re_{SL}\right)_{crit} = (0.29 \pm 0.06) \times 10^6$$

It is shown by Kabelitz (Ref. 8) that for Mach numbers at or below $M_\infty = 2$ the experimental data scatter as much as a factor of 2 or more in regard to the value of

[#] The static effect is the opposite, i.e., statically stabilizing, which is explained at length in Reference 5.

[##] L_S/D is an important parameter in addition to its influence on M_e in Eq. (21).

$(L_S/D)_{crit}$ for similar Reynolds numbers. Thus, it probably is coincidental that Mair's data point, $(L_S/D)_{crit} = 1.3$ for $M_\infty = 1.96$, fits on the curve in Figure 21. Another way to accomplish this stretching of the shear layer profile is to use a "hammerhead" spike tip and let the mixing with the "dead air" base flow region do the work. Beastall and Turner (Ref. 36) have demonstrated how this can eliminate the flow unsteadiness (Fig. 22). Reeves accomplished the same thing by letting a ring suspended in the shear layer (upstream of reattachment) do the mixing (Ref. 33).

In the case of the forward facing cavity, e.g., the empty SRM-nozzle (Fig. 2), control of flow pulsation can also be carried out in a manner similar to what has been discussed for the spiked body. Although the frequency dependence on geometry is less well established it should often be possible to make sure that resonance with a structural mode is avoided by using Eqs. (18) and (19). In regard to the possibility to inhibit or moderate flow pulsations both external and internal nozzle geometry are important. It is clear that steady flow can only exist as long as the bow shock stays external to the nozzle. The maximum flow inclination for which this will occur can be increased by "bluntening up" the nozzle exterior. When the unsteadiness finally occurs at a higher flow inclination than before, the associated unsteady loads should be less than before. Using the projected free stream velocity component on the nozzle axis as a measure one would expect the sound pressure level to vary as the n'th power of the cosine of the flow inclination, where $n > 1$.

The internal nozzle geometry has also a large influence on the pulsating flow phenomenon. It was discussed earlier what the effect was of going from a cylindrical to a conic cavity. Johnson (Ref. 28) also showed that a hemispherical internal nozzle shape caused flow unsteadiness even without mass addition. The unsteadiness was of the rotating type observed on the cylindrical cavity with mass addition except for "snaps into stable position for short intervals." With mass addition in the center of the cavity bottom a seemingly steady asymmetric bow shock configuration was obtained (at $\alpha = 0$) which looked very similar to the "end-stroke position (most forward) of the bow shock geometry obtained on the SRM-nozzle at large flow inclination (Fig. 2). Johnson's results are for extremely high Mach numbers, $M_\infty > 21$. However, similar results for hemisphere cavities have been obtained in other investigations at

supersonic Mach numbers (Refs. 37 and 38). At $M_\infty = 1.98$ Cooper et al (Ref. 37) found a pseudo-stable flow condition, i.e., the bow shock would stay in the symmetric or asymmetric configuration for long time periods with the change between the two states coming at random intervals (Fig. 23). Markley (Ref. 39) could, however, only obtain the symmetric stable shock configuration. At $M_\infty = 4.95$ Cooper et al obtained the oscillatory asymmetric pulsating shock configuration that Johnson observed (Ref. 28). The Strouhal number based on face diameter was $S_D = 0.099$.

Demetriades (Ref. 26) and Cassanto et al (Ref. 40) have tested tension shell type geometrics that combine some of the geometric features of spiked bodies and forward facing cavities (Fig. 24). The data points for the regular symmetric pulsating flow phenomenon agree well with the predictions from Eq. (17), as does also the experimental data obtained by Baltakis (Ref. 41). Both Demetriades and Cassanto et al observed also an asymmetric pulsating flow phenomenon very similar to that discussed here earlier for forward facing cavities. The frequency of this rotating (according to Demetriades) or rocking (according to Cassanto et al) pulsating flow phenomenon was observed to be half that of the symmetric pulsating flow. Using Eq. (18) one computes for a hemispherical cavity at $M_\infty = 4.95$ the Strouhal number $S_{LS} = 0.088$. Using half this frequency[#] gives $S_D = 0.088$ which is in rather good agreement with the value $S_D = 0.099$ measured by Cooper et al (Ref. 37).

Stallings and Burbank (Ref. 38) observed at $M_\infty = 2.49$ and $M_\infty = 3.5$ the same pseudo-steady bow shock condition that Cooper et al (Ref. 37) found at $M_\infty = 1.98$, and obtained the asymmetric flow pulsation at $M_\infty = 4.44$ for the whole angle-of-attack range tested, $0 \leq \alpha \leq 15°$. However, they did not measure the frequency of the flow pulsations. This unsteady flow phenomenon is of great concern when designing a drag device for use at supersonic speeds (Ref. 42). In that case the design solution is to combine the "hammerheaded" spike tip effect (Fig. 22) with an opening for partial through-flow at the bottom of the cavity. Although it is obvious that viscous effects play a dominant role in setting up these unsteady flows, there is some indication that unstable inviscid flow processes also play a role (Ref. 43).

[#] Noting that $\frac{L_S}{D} + \frac{h_C}{D} - \frac{\Delta_{sh}}{D} = \frac{h_C}{D} = \frac{1}{2}$ in Eq. (18).

In the case of the SRM-nozzle "flying backwards" (Figs. 1 and 2) some "through flow" at the base of the cavity is a possibility. However, it will more than likely be of much more complicated character than in the case of the "through flow" parachute (Ref. 42). From geometric considerations one is likely to incorporate a new unsteady phenomenon, that associated with the so-called resonance tube (Ref. 44). This will also be the case if the cavity is not shallow, as has been assumed in the discussion so far. Figure 25a shows a series of flow photographs illustrating the various stages in one cycle of the oscillation taking place in the two-dimensional resonance tube used by Vrebavolich (Ref. 44). The "flow trip" starting the oscillation, or at least greatly amplifying it, is a two-dimensional spike or what Vrebavolich calls a "wing-trip." Frame 1 shows the "swallowing" of the normal shock with completely separated flow up to the spike tip. In Frame 2 the spike flow is almost fully attached while the shock, after reflection off the bottom of the tube, is moving upstream. This is the compression phase of the oscillation (see Fig. 25b)[#]. In Frame 3 the shock is being "spilled" starting the spike flow separation which in Frame 4 has reached the spike tip and remains there in Frame 5, while the tube is still "spilling" air. In Frame 6 the expansion or "swallowing" phase is just about to begin. Figure 25b shows that the strong shock reached the spike tip between Frames 5 and 6, as is indicated by the steepening of the spike tip shock (strength) (see top graph in Fig. 25b).

Comparing Figure 25a with Figure 3a one can see great similarities. The big difference is that in Figure 25a, i.e., in the presence of a very deep forward facing cavity, the period of the oscillation cycle is determined by the filling and spilling process of the tube or cavity. This time period is that corresponding to the organ pipe oscillation with the wave length equal to four tube lengths[##]. Thus, the corresponding Strouhal number is in this case

$$\frac{f\,h_C}{U_\infty} = \frac{1}{4}\left(\frac{\gamma - 1}{\gamma + 1}\right)^{1/2}\left[1 + \frac{2}{(\gamma - 1)\,M_\infty^{\,2}}\right]^{1/2} \tag{22}$$

[#]The numbers in Fig. 25b indicate where the flow pictures in Fig. 25a belong.

[##]This is with the tube closed at the downstream end. With it open the wave length for the ground tone would be two tube lengths.

With $h_C = 10$ inches the measured frequency (Ref. 44) gave $f\,h_C/U_\infty = 0.122$ whereas Eq. (22) gives $f\,h_C/U_\infty = 0.130$. Using Eq. (22) one obtains for $\bar{S}_{LS}$

$$\bar{S}_{LS} = \frac{1}{4}\left(\frac{\gamma - 1}{\gamma + 1}\right)^{1/2}\left[1 + \frac{2}{(\gamma - 1)\,M_\infty^{\,2}}\right]^{1/2}\left(1 + \frac{L_S}{h_C}\right) \qquad (23)$$

In Figure 26 the experimental results for $M_\infty = 3.5$ and $L_S/D = 0.9$ (Ref. 26) are compared with the predictions obtained from Eq. (18) and Eq. (23). It is obvious that for shallow cavities, $h_C/D < 1$, the convective processes dominating the spiked body flow pulsation still are in control. For deep cavities, $h_C/D > 1$, the acoustic fill-spill cycle of the cavity, the organ-pipe phenomenon, takes over the control. It is worthwhile noting that the asymptotic value $\bar{S}_{LS} = 0.121$ is the constant value that would apply if one assumed that the flow recirculation on the spike also was acoustically controlled. It is clear that this cannot be the case, especially when considering the rest of the experimental data (Fig. 17). One would be inclined to conclude from Figure 26 that as long as the convective flow processes on the spike and cavity inlet (shallow cavity) are slower than the acoustic processes in the rest of the cavity (deep cavity), the flow oscillation frequency is given by Eq. (18). Conversely, when the acoustic cavity process takes the longest time ($h_C/D > 1.15$ in Figure 26) the oscillation frequency is given by Eq. (23) or Eq. (22).

Figure 25a illustrates the situation often existing for supersonic inlets, a similarity that has been utilized to analyze inlet buzz (Ref. 45). To what extent it applies to the interference flow field between orbiter and booster (HO tanks and SRM's) on the space shuttle launch vehicle is a moot question because of the spanwise spillage and the presence of exhaust plumes (Fig. 26). The flow in deep forward facing cavities can also become oscillatory without using the spike as a tripping device for the unsteadiness. The higher than stagnation value heating of the bottom of these resonance tubes have very useful practical applications, and extensive studies have been made of them. A recent review of the field is contained in Reference 46, which also shows that the oscillatory flow exists even at high subsonic speeds, i.e., in absence of the strong moving shocks in the tube which have been thought to be necessary. The authors have no explanation for this but speculate that there must be some interaction between viscous and acoustic processes (also in absence of shocks) that sets up the

oscillation and associated heating amplification, which in their test was as high for this subsonic condition as for the various supersonic cases investigated. In the unsteady flow occurring in sideward facing cavities the situation is somewhat similar to that for spiked forward facing cavities, i.e., convective shear layer processes compete with cavity acoustics in regard to the control of the oscillation and its frequency. (See Ref. 47 for a thorough and up-to-date review of the field.) The flow oscillations are only observed in what Charwat et al (Ref. 48) have termed "open cavities," i.e., cavities in which flow reattachment occurs only on the downstream cavity shoulder[#]. Thus, it is not surprising to find that a softening of this reattachment through slanting the aft cavity wall backwards is the most effective means of suppressing the oscillations (Ref. 47). The same was true for the spike induced oscillations (Refs. 8 and 11).

[#]This sets an upper limit on the length-to-depth ratio for the cavity.

Section 3
UNSTEADY AERODYNAMICS

In earlier studies the effect of the spike-induced separated flow on the aerodynamic damping has been determined (Refs. 5, 49, and 50), and in a more recent investigation also the forcing function off "hammerheaded" spikes has been studied (Refs. 51 and 52). In the present analysis only the unsteady aerodynamics of the "backward flying" SRM's will be considered.

3.1 Cavity Flow Pulsations

Figure 28 shows the innermost shock position before the start of a pumping cycle. In Figure 28a the real flow is sketched with internal oblique shocks non-parallel with the nozzle walls and with the normal shock a finite distance above the nozzle bottom. In Figure 28b the idealized flow is shown with oblique shocks parallel with the walls and the normal shock an infinitesimal distance above the "floor." This is the Newtonian type idealization. Using the definitions in Figure 29 and the generalized embedded Newtonian theory of Reference 53 the analysis can proceed in the following manner.

Assuming a two-dimensional type behavior for the internal flow one can according to Reference 54 assume that $\rho U^2 = \rho_\infty U_\infty^2$ and that C_{po} is a function of x only. Thus, with $V_\perp/U$ defined as before (see Ref. 53 with $\theta_F = -\theta_R$).

$$
\left.
\begin{aligned}
C_p &= \begin{cases} C_{po} + C_{p_{MAX}} \left(\dfrac{V_L}{U_\infty}\right)^2 & : \phi > \phi' \\ C_{po} & : \phi' \leq \phi \end{cases} \\
\frac{V_L}{U} &= \sin\alpha' \cos\theta_R \sin\phi - \cos\alpha' \sin\theta_R \\
\phi' &= \sin^{-1}\left(\frac{\tan\theta_R}{\tan\alpha'}\right) \\
\alpha' &= \pi - \alpha \\
C_{pMAX} &\approx 1.8
\end{aligned}
\right\} \qquad (24)
$$

When the strong shock has passed upstream over the area element the pres s given by the normal shock relations (Ref. 18). In the case of steady hypersonic flow the shock strength is

$$C_{\hat{p}_o} = \frac{4}{\gamma + 1}\left(1 - \frac{1}{M_\infty^2}\right) \approx \frac{4}{\gamma + 1} \qquad (25)$$

In the nonsteady case the shock strength can be written

$$C_{\hat{p}_{NS}} \approx \frac{4}{\gamma + 1}\left(1 + \frac{\Delta M_{NS}}{M_\infty}\right)^2 \qquad (26)$$

where $\Delta M_{NS} > 0$ for the pumping phase when the shock moves upstream and $\Delta M_{NS} < 0$ for the expansion phase when the shock moves downstream. For deeper cavities the results obtained by Vrebavolich (Fig. 25 and Ref. 44) indicate the following values $C_{\hat{p}_u}$ and $C_{\hat{p}_d}$ for the shock strength during the upstream and downstream movement respectively.

$$
\left.
\begin{aligned}
0 < C_{\hat{p}_d} &< 0.25\, C_{p_o} \\
C_{\hat{p}_d} < C_{\hat{p}_u} &< C_{\hat{p}_o}
\end{aligned}
\right\} \qquad (27)
$$

Thus, the pressure on the internal nozzle wall will vary with time as is illustrated in Figure 30. In the steady case the pressure is $C_{\hat{p}o}$ throughout the nozzle, where $C_{\hat{p}o} < C_{\hat{p}u}$. The pressure change in the unsteady case from the steady state level is $\Delta C_p = C_{pu} - C_{\hat{p}o}$, where C_{pu} is given by either of Eqs. (21), (26), or (27) depending upon where in the oscillation cycle the nozzle is (Fig. 30). The corresponding change in the strip loading is (see Fig. 29).

$$\frac{d\Delta C_A}{dr} = -\frac{2r}{S} \times \begin{cases} \displaystyle\int_{-\pi/2}^{\pi/2} (C_{\hat{p}u} - C_{\hat{p}o})\, d\phi & ; \quad t_o \le t < t_1 \\ \displaystyle\int_{-\pi/2}^{\pi/2} (C_{\hat{p}d} - C_{\hat{p}o})\, d\phi & ; \quad t_1 \le t < t_2 \\ \displaystyle\int_{-\pi/2}^{\pi/2} (C_{p}^{\vee} - C_{\hat{p}o})\, d\phi & ; \quad t_2 \le t < t_3 \end{cases} \tag{28}$$

$$\frac{d\Delta C_N}{dx} = \frac{2r}{S} \times \begin{cases} \displaystyle\int_{-\pi/2}^{\pi/2} (C_{\hat{p}u} - C_{\hat{p}o}) \sin\phi\, d\phi & ; \quad t_o \le t < t_1 \\ \displaystyle\int_{-\pi/2}^{\pi/2} (C_{\hat{p}d} - C_{\hat{p}o}) \sin\phi\, d\phi & ; \quad t_1 \le t < t_2 \\ \displaystyle\int_{-\pi/2}^{\pi/2} (C_{p}^{\vee} - C_{\hat{p}o}) \sin\phi\, d\phi & ; \quad t_2 \le t < t_3 \end{cases} \tag{29}$$

Integrating Eqs. (28) and (29) utilizing Eqs. (24) - (27) gives

$$\frac{d\Delta C_A}{dr} = \frac{2\pi r}{S} \times \begin{cases} C_{\hat{p}o} - C_{\hat{p}u} & ; \quad t_o \leq t < t_1 \\ C_{\hat{p}o} - C_{\hat{p}d} & ; \quad t_1 \leq t < t_2 \\ C_{\hat{p}o} - C_{po} - \dfrac{C_{pMAX}}{\pi} \left[\left(\dfrac{\pi}{2} + \phi' \right) \left(\cos^2 \alpha' \sin^2 \theta_R + \dfrac{1}{2} \sin^2 \alpha' \cos^2 \theta_R \right) + \dfrac{1}{2} \sin 2\alpha' \sin 2\theta_R \cos \phi' \right] & ; \\ t_2 \leq t < t_3 \end{cases} \tag{30}$$

$$\frac{d\Delta C_N}{dx} = -\frac{2r}{S} C_{p_{MAX}} \times \begin{cases} 0 & ; \quad t_o \leq t < t_1 \\ 0 & ; \quad t_1 \leq t < t_2 \\ \left(\dfrac{\pi}{2} + \phi' - \dfrac{1}{2} \sin 2\phi' \right) \dfrac{1}{4} \sin 2\alpha' \sin 2\theta_R \\ \quad + \cos \phi' \left[\cos^2 \alpha' \sin^2 \theta_R \right. \\ \quad \left. + \sin^2 \alpha' \cos^2 \theta_R \left(1 - \dfrac{1}{3} \cos^2 \phi' \right) \right] & ; \quad t_2 \leq t < t_3 \end{cases} \tag{31}$$

From Figure 30 one can define the time duration during one cycle for the different pressure levels[#].

$$\left.\begin{aligned} (t_1 - t_o)/T &= \left(x + \Delta_{sh}\right)/(h_C + \Delta_{sh}) \left(1 + \bar{U}/U_\infty\right) \\ (t_2 - t_1)/T &= \left(x + \Delta_{sh}\right)/(h_C + \Delta_{sh}) \left(1 + U_\infty/\bar{U}\right) \\ (t_3 - t_2)/T &= (h_C - x)/(h_C + \Delta_{sh}) \end{aligned}\right\} \tag{32}$$

[#]Note that the assumption of non-finite distance between normal shock and nozzle bottom at the start of the cycle will have a negligible influence on the computed time average loads.

If the nozzle walls are thin or the nozzle lips are relatively sharp one can neglect C_{po} (Refs. 53 and 54). This simplifies the computation of the time average load change from the steady state condition. Combining Eqs. (25) - (27) with Eqs. (30) and (31) gives the following integrated result.

$$\overline{\Delta C}_A = \frac{\pi D_I^2}{4S} \frac{D_I \cot \theta_R}{6 (h_C + \Delta_{sh})} \left\{ \left\{ \left\{ 2 - \frac{d_i}{D_I} \left[3 - \left(\frac{d_i}{D_I} \right)^2 \right] \right\} \right. \right.$$

$$\left\{ C_{\hat{p}o} - \frac{C_{pMAX}}{\pi} \left[\left(\frac{\pi}{2} + \phi' \right) \left(\cos^2 \alpha' \sin^2 \theta_R \right. \right. \right.$$

$$\left. \left. + \frac{1}{2} \sin^2 \alpha' \cos^2 \theta_R \right) + \frac{1}{2} \sin 2\alpha' \sin 2\theta_R \cos \phi' \right] \right\}$$

$$\left. \left. + \left(1 + 6 \frac{\Delta_{sh}}{D_I} \tan \theta_R \right) \left[(C_{\hat{p}o} - C_{\hat{p}u}) + \frac{\overline{U}}{U_\infty} (C_{\hat{p}o} - C_{\hat{p}d}) \right] \middle/ \left(1 + \frac{\overline{U}}{U_\infty} \right) \right\} \right\} \quad (33)$$

$$\overline{\Delta C}_N = \frac{h_C^2 C_{pMAX}}{S (h_C + \Delta_{sh})} \left(\frac{D_I}{2} - \frac{h_C}{3} \tan \theta_R \right) \left\{ \left(\frac{\pi}{2} + \phi' \right. \right.$$

$$\left. - \frac{1}{2} \sin 2\phi' \right) \frac{1}{4} \sin 2\alpha' \sin 2\theta_R + \cos \phi' \left[\cos^2 \alpha' \sin^2 \theta_R \right.$$

$$\left. \left. + \sin^2 \alpha' \cos^2 \theta_R \left(1 - \frac{1}{3} \cos^2 \phi' \right) \right] \right\} \quad (34)$$

The corresponding change of the pitching moment is

$$\left. \begin{aligned} \overline{\Delta C_m} &= (\bar{x} - x_{CG}) \Delta C_N \\ \bar{x} &= \frac{h_C}{3} \frac{\frac{D_I}{2} - \frac{h_C}{2} \tan \theta_R}{\frac{D_I}{2} - \frac{h_C}{3} \tan \theta_R} \end{aligned} \right\} \quad (35)$$

Eq. (2) defines $\bar{U}/U_\infty = \bar{U}_u/U_\infty$ as

$$\bar{U}/U_\infty = \left[\bar{S}_{LS}^{-1} - 1\right]^{-1} \tag{36}$$

The discontinuous changes of the aerodynamic characteristics caused by the flow pulsations are shown in Figure 31, complementing the C_m - results already shown in Figures 1 and 2. The magnitude of the C_N - discontinuity is not measurable. However the C_A - and C_m - discontinuties are. Figure 32 shows the measured discontinuities for three different nozzle geometries (Refs. 2 and 3). Also shown are the time average values predicted from the present analysis.[#] The agreement between predicted and measured discontinuities is very satisfactory. Although it may be desirable to be able to predict these time average effects on the static aerodynamic characteristics, the more significant impact of Figure 32 is that it lends credibility to the very simple unsteady flow model suggested for the pulsating flow process. Thus, it should be possible to use the present model in an analysis to determine whether or not the pulsating flow phenomenon will endanger the structural integrity of the rocket nozzle on the jettisoned, empty SRM-shells.

[#] From Eq. (27) the values $C_{\hat{p}d} = 0$ and $C_{\hat{p}u} = C_{\hat{p}o}$ were chosen for simplicity.

Section 4
CONCLUSIONS

A study of the unsteady aerodynamics of bodies with concave nose geometrics has shown the following.

- The spike-induced flow separation remains steady as long as the recompression at reattachment can be accomplished by (a series of) oblique shocks.
- This is the case if either the spike is long enough or the surface inclination at reattachment is mild enough.
- No unsteady spike-induced flow separation exists if the Reynolds number is below a critical value or the free shear layer is thicknened artificially to a corresponding degree.
- If the face is in lined forward, creating a forward facing cavity, the unsteady spike-induced flow separation persists even for very long spikes.
- Unsteady flow exists on forward facing cavities even in absence of a spike. At zero angle of attack without mass addition it has been observed only for a hemispherical cavity. However, at moderately high angles of attack (at which the windward branch of the bow shock moves into the cavity) a pulsating flow phenomenon exists which is very similar to that observed in cavities with a flow separation spike present.
- Simple analytic means are developed by which the experimentally observed oscillation frequency of the pulsating flow can be predicted both for spiked bodies and forward facing cavities.
- The postulated mathematic model for the pressure time history of the pulsating flow gives time average results that are in good agreement with the measured discontinuities in static tests. This strongly implies that the structural integrity of the SRM-nozzle in presence of pulsating flow could be determined analytically.

REFERENCES

1. Fink, D.A., "Space Shuttle Flight Plan Written," Aviation Week & Space Technology, June 3, 1974, pp 12-15.

2. Johnson, J.D., and Radford, W.D., "Aerodynamic Characteristics of a 142-Inch Diameter Solid Rocket Booster," NASA CR-128, 774, Aug. 1973.

3. Clover W.W., Private Communication of Unpublished Data, NASA Marshall Space Flight Center, Nov. 1975.

4. Ericsson, L.E., and Reding, J.P., "Analysis of Flow Separation Effects on the Dynamics of a Large Space Booster," J. Spacecraft and Rockets, Vol. 2, No. 2, July-August 1965, pp 481-590.

5. Ericsson, L.E., and Reding, J.P., "Dynamics of Separated Flow over Blunt Bodies," Technical Summary Report 2-80-65-1, Contract NAS 8-5338, Nov. 1962, Lockheed Missiles & Space Company, Inc., Sunnyvale, California.

6. Ericsson, L.E., "Unsteady Characteristics of a Spiked Bluff Body," LMSC-804651, Contract NAS 8-5338, July 1964, Lockheed Missiles & Space Company, Inc., Sunnyvale, California (C).

7 Ericsson, L.E., "Steady Loads on Spiked Blunt Bodies of Revolution," LMSC TM 53-40-121 (LMSC-A312114), Contract NAS 8-5338, Nov. 1962, Lockheed Missiles & Space Company, Inc., Sunnyvale, California (C).

8. Kabelitz, H-P., "Zur Stabilität geschlossener Grenzschichtablösegebiete an Konischen Drehkörpern bei Hyperschallanströmung," DLR FB 71-77, July 1971.

9. Kabelitz, H-P., "Zur Stabilität geschlossener Grenzschichtablösegebiete bei Über-und Hyperschallanströmung," Vortrags-Nr. 71-065, 4. Jahrestagung der DGLR, Baden-Baden, W. Germany, 11-13 Oct. 1971.

10. Album, H. H., "Spiked Blunt Bodies in Supersonic Flow," Report No. AFOSR 307, June 1961.

11. Maull, D.J., "Hypersonic Flow over Axially Symmetric Spiked Bodies," J. of Fluid Mechanics, Vol. 8, Part 4, Aug. 1960, pp 584-594.

12. Settles, G.S., Bogdonoff, S.M., and Vas, I.E., "Incipient Separation in Supersonic Turbulent Boundary Layer," AIAA Paper No. 75-7, Jan. 1975.

13. Elfstrom, G.M., "Turbulent Separation in Hypersonic Flow," Imperial College Aero Report 71-16, Sept. 1971.

14. Holden, M.S., "Shock Wave-Turbulent Boundary Layer Interaction in Hypersonic Flow," AIAA Paper 72-74, Jan. 1972.

15. Reding, J.P., and Ericsson, L.E., "Effects of Delta Wing Separation on Shuttle Dynamics," J. of Spacecraft and Rockets, Vol. 10, No. 7, July 1973, pp 421-428.

16. Reding, J.P., and Ericsson, L.E., "Review of Delta Wing Space Shuttle Dynamics," Technology Conference, Vol. III - Aerodynamics, TMX-2508, Feb. 1972, NASA, pp 861-921.

17. Reding, J.P., and Ericsson, L.E., "Review of Delta Wing Space Shuttle Vehicle Dynamics," Report LMSC-D2432938, Contract NAS 9-11495, Oct. 1971, Lockheed Missiles & Space Company, Inc., Sunnyvale, California.

18. Ames Research Staff, "Equations, Tables, and Charts for Compressible Flow," Report 1135, 1953. NACA

19. Eggers, A.J., and Hermach, C.A., "Initial Experiments on the Aerodynamic Cooling Associated with Large-Scale Vortical Motions in Supersonic Flow," RM A54L13, March 1955, NACA.

20. Daniels, L.E., and Yoshihara, H., "Effect of the Upstream Influence of a Shock Wave at Supersonic Speeds in the Presence of a Separated Boundary Layer," WADC TR No. 54-31, Jan. 1954, Wright Air Development Center, Wright Patterson AFB, Ohio.

21. Kabelitz, H-P., Wyborny, W. and Schepers, H-J., "Untersuchungen über den Wärmeübergang am Zentralstift von stumpfen Körpern," DLR Mitt. 67-13, 1967, pp 92-124.

22. Serbin, H., "Supersonic Flow Around Blunt Bodies," Journal of Aerospace Sciences, Vol. 25, No. 1, Jan. 1958, pp 58-59.

23. Mair, W.A., "Experiments on Separation of Boundary Layers on Probes in Front of Blunt-Nosed Bodies in a Supersonic Air Stream," Philosophical Magazine, Vol. 43, 1952, pp 695-716.

24. Kutterer, R.E., "Pulsationen der Strömung um Flugkörper," ISL-Kolloquim 8/60, 1960.

25. Abbet, M.J., Cooper, L., Dahm, T.J., and Jackson, J.O., Jr., "Flow Characteristics about Concave Conic Forebodies at High Mach Numbers," AIAA Paper No. 75-153, Jan. 1975.

26. Demetriades, A., and Laderman, A.J., "Advanced Penetration Problems Program, Final Report, Vol. 1," SAMSO TR NO 75-51, Dec. 1974.

27. Hermach, C.A., Kraus, S., and Reller, J.O., Jr., "Reduction in Temperature-Recovery Factor Associated with Pulsating Flows Generated by Spike-Nosed Cylinders at Mach Number of 3.50," RM A56L05, March 1957, NACA.

28. Johnson, R.H., "Instability in Hypersonic Flow about Blunt Bodies," The Physics of Fluids, Vol. 2, No. 5, Sept.-Oct. 1959, pp 526-532.

29. Navone, M.V., "Results of Pressure Tests on Rearward Facing Polaris Reentry Bodies in the AEDC/VKH Tunnel B (R-103)," TM 57-11-67, LMSC/656605, June 1962, Lockheed Missiles & Space Company, Sunnyvale, California.

30. Lucero, E.F., "Turbulent Boundary-Layer Separation Induced by Three-Dimensional Protuberances," Tech. Mem. TG 1094, John Hopkins University, Jan. 1970.

31. Sedney, R., "The Effect of Steady Three-Dimensional Perturbations in Boundary Layers," BRL Rpt. No. 1748, Nov. 1974.

32. Sedney, R., "Detailed Study of a Separated Turbulent Boundary Layer in High Reynolds Number Supersonic Flow, ' AIAA Paper No. 76-164, Jan. 1976.

33. Reeves, B.L., Private communication of unpublished results, Nov. 1974.

34. Wood, C.J., "Hypersonic Flow over Spiked Cones," J. Fluid Mech., Vol. 12, 1962, pp 614-624.

35. Ericsson, L.E., "Entropy Gradient Effects on Blunted Cone Transition," AIAA Paper No. 75-195, Jan. 1975.

36. Beastall, D., and Turner, J., "The Effect of a Spike Protruding in Front of a Bluff Body at Supersonic Speeds," ARC Reports and Memoranda No. 3007, Jan. 1952.

37. Cooper, M., Beckwith, I.E., Jones, J.J., and Gallagher, J.J., "Heat Transfer Measurements on a Concave Hemispherical Nose Shape with Unsteady-Flow Effects at Mach Numbers of 1.98 and 4.95," NACA RML 58D25a, July 1958.

38. Stallings, R.L., Jr. and Burbank, P.B., "Heat-Transfer and Pressure Measurements on a Concave-Nose Cylinder for a Mach Number Range of 2.49 to 4.44," NASA TMX-221, Oct. 1959.

39. Markley, J.T., "Heat Transfer and Pressure Measurements on a 5-Inch Hemispherical Concave Nose at a Mach Number of 2.0," NACA RM L58C14a, July 1958.

40. Cassanto, J.M., Monfort, A., and Fehl, C., "An Experiment to Determine the Existence of R/V Nosetip Transient Shocks," AIAA Paper No 76-54, Jan. 1976.

41. Baltakis, F.P., "Wind-Tunnel Study of Oscillating Flow-Induced Surface Pressures on a Tension-Cone Geometry Model," NOL TR 74-134, Jan. 1974.

42. Heinrich, H.G., "Aerodynamics of the Supersonic Guide Surface Parachute," Journal of Aircraft, Vol. 3, No. 2, March-April 1966, pp 105-111.

43. Bastianon, R.A., "Unsteady Solution of the Flowfield over Concave Bodies," AIAA Journal, Vol. 7. No. 3, March 1969, pp 531-533.

44. Vrebalovich, T., "Resonance Tubes in a Supersonic Flow Field," J.P.L. TR/No. 32-378, July 1962.

45. Dailey, C.L., "Supersonic Diffuser Instability," Journal Aerospace Sci., Vol. 22, No. 11, Nov. 1955, pp 733-749.

46. Przirembel, C.E.G., Wolf, D.E., and Fletcher, L.S., "Thermodynamic Characteristics of a Blunt, Two-Dimensional Resonance Tube," AIAA Paper No. 76-145, Jan. 1976.

47. Heller, H.H., and Bliss, D.B., "Aerodynamically Induced Pressure Oscillations in Cavities - Physical Mechanism and Suppression Concepts," AFFDL-TR-74-133, Feb. 1975.

48. Charwat, A.F., Roos, J.N., Dewey, F.C., Jr., and Hitz, J.A., "An Investigation of Separated Flows - Part I: The Pressure Field," J. Aero. Sci., Vol. 28, No. 6, June 1961, pp 457-470.

49. Reding, J.P., and Ericsson, L.E., "Loads on Bodies in Wakes," J. Spacecraft and Rockets, Vol. 4, No. 4, April 1967, pp 511-518.

50. Reding, J.P., "Forces Induced on Bodies in Free Wakes and Three-Dimensional Cavities, LMSC-804651, Contract NASA 81-5338, Sunnyvale, California, Dec. 1965.

51. Guenther, R.A., "Analysis of the Fluctuating Pressure Test of the C4A Candidate Nose Fairing (E-82)," LMSC Report LMSC/D366982, April 1975.

52. Reding, J.P., and Guenther, R.A., "Unsteady Aerodynamic Considerations in the Design of a Drag Reduction Spike," Proceedings of the 17th Structures, Structural Dynamics and Materials Conference, King of Prussia, Pennsylvania, May 5-7, 1976.

53. Ericsson, L.E., "Generalized Unsteady Embedded Newtonian Flow," AIAA Paper No. 75-210, Jan. 1975.

54. Ericsson, L.E., Almroth, B.O., Bailie, J.A., Brogan, F.A., and Stanley, G.M., "Hypersonic Aeroelastic Analysis," LMSC Report LMSC-D056746, Contract N62269-73C-0713, Sept. 1975.

Appendix A
NOMENCLATURE

A	axial force: coefficient $C_A = A/(\rho_\infty U_\infty^2/2)\ S$
a	speed of sound
c	reference length (SRM-diameter)
D	body diameter (Fig. 10)
$\bar{D}$	reattachment diameter (Fig. 10)
D_o, $\bar{D}_o$	idealized reattachment parameters (Fig. 9)
d_i, D_I	internal nozzle diameters (Fig. 29)
D_F	diameter of flat face area (Fig. 11)
d_S	spike diameter (Fig. 10)
f	oscillation frequency
h_C	cavity depth (Fig. 17)
K_c	boundary layer parameter, Eq. (20)
K_{SL}	free shear layer parameter, Eq. (21)
L, $\bar{L}$	spike length definitions (Fig. 10)
L_S	spike length for flat faced bodies, $L_S = L = \bar{L}$
M	Mach number, $M = U/a$
M_p	pitching moment: coefficient $C_m = M_p/(\rho_\infty U_\infty^2/2)\ Sc$
N	normal force: coefficient $C_N = N/(\rho_\infty U_\infty^2/2)\ S$
p	static pressure: coefficient $C_p = (p - p_\infty)/(\rho_\infty U_\infty^2/2)$
p_o	blast wave pressure

Re	Reynolds number
Re_D	Re based on D and free stream conditions
r	radius of shoulder roundness
S	reference area, $S = \pi c^2/4$
S_D, S_{Ls}	Strouhal number, $S_D = fD/U_\infty$, $S_{Ls} = f L_S/U_\infty$
T	oscillation period
t	time
Δt	time lag
U	axial velocity
V_L	velocity component normal to surface element
X_ℓ	parameter defined in Eq. (17)
x	axial body-fixed coordinate (Fig. 29)
α	angle of attack
α'	α-complement, $\alpha' = \pi - \alpha$
γ	ratio of specific heats, $\gamma = 1.4$ in air
Δ	increment
Δ_{sh}	shock standoff distance
δ	boundary layer thickness
δ_{SL}	thickness of free shear layer
θ_c	spike tip cone angle (Fig. 10)
θ_R	slope of nozzle wall (Fig. 29)
ρ	air density
ϕ	azimuth (Fig. 29)
ϕ'	ϕ-value for Newtonian shadow, Eq. (25)

Subscripts

E	external
e	edge of boundary layer or free shear layer
eff.	effective value
I, i	internal
'	linear-tangential extension
MAX	maximum
NS	nonsteady
OPT	optimum
S	spike
SL	shear layer
SRM	Solid Rocket Motor
u	upstream
uc	upstream convection
0, 1, 2, 3	phases in oscillation cycle (Fig. 30)
∞	free stream condition

Superscripts

(*)	value (hypothetical) for optimum spike length
(-)	barred quantities denote integrated mean or time average values
($\wedge$)	"roof" indicates value behind a normal shock
($\vee$)	"inverted roof" indicates embedded Newtonian value

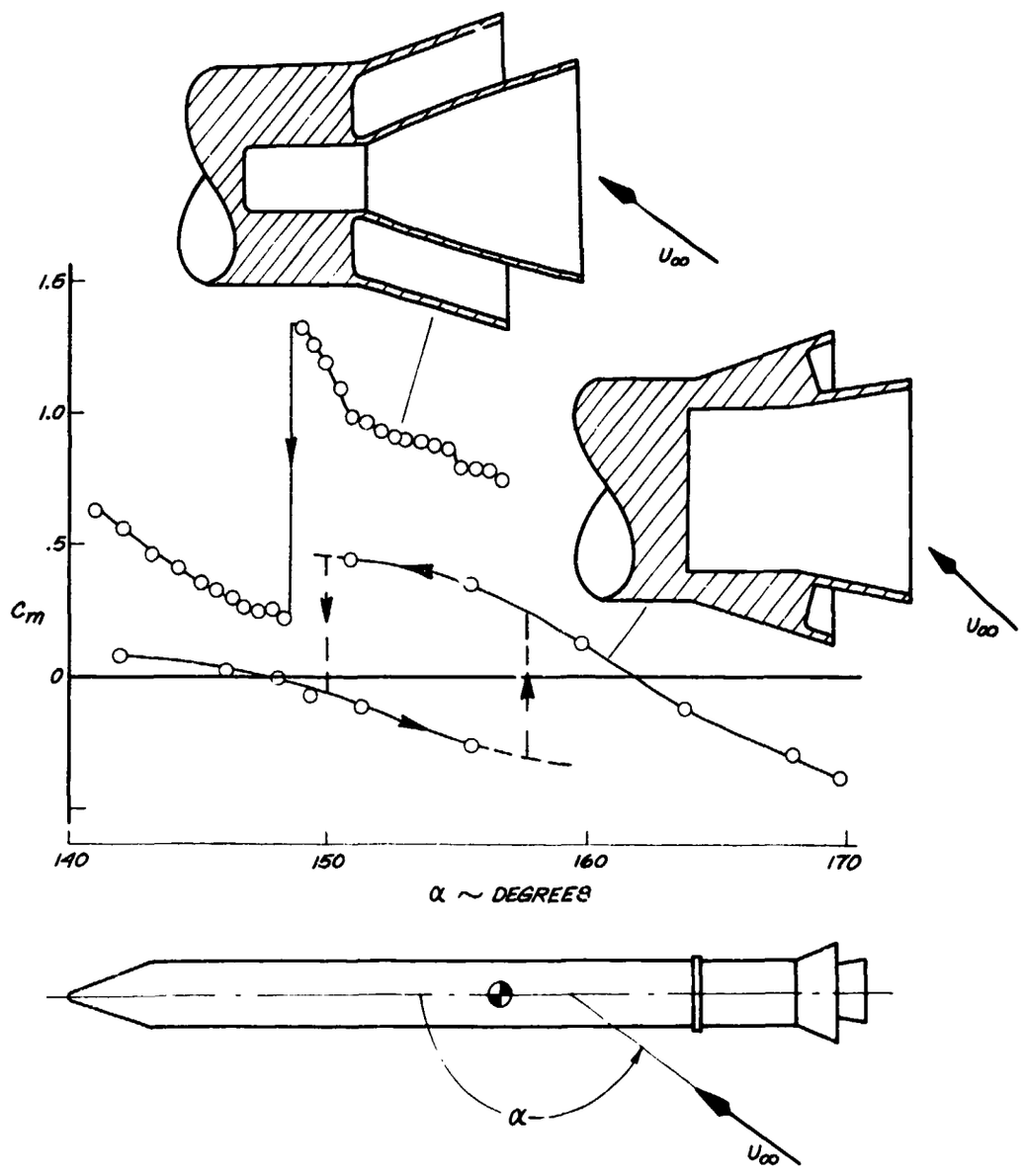

Figure 1 Pitching Moment of SRM's at $M_\infty = 3.48$ and $140° < \alpha < 180°$

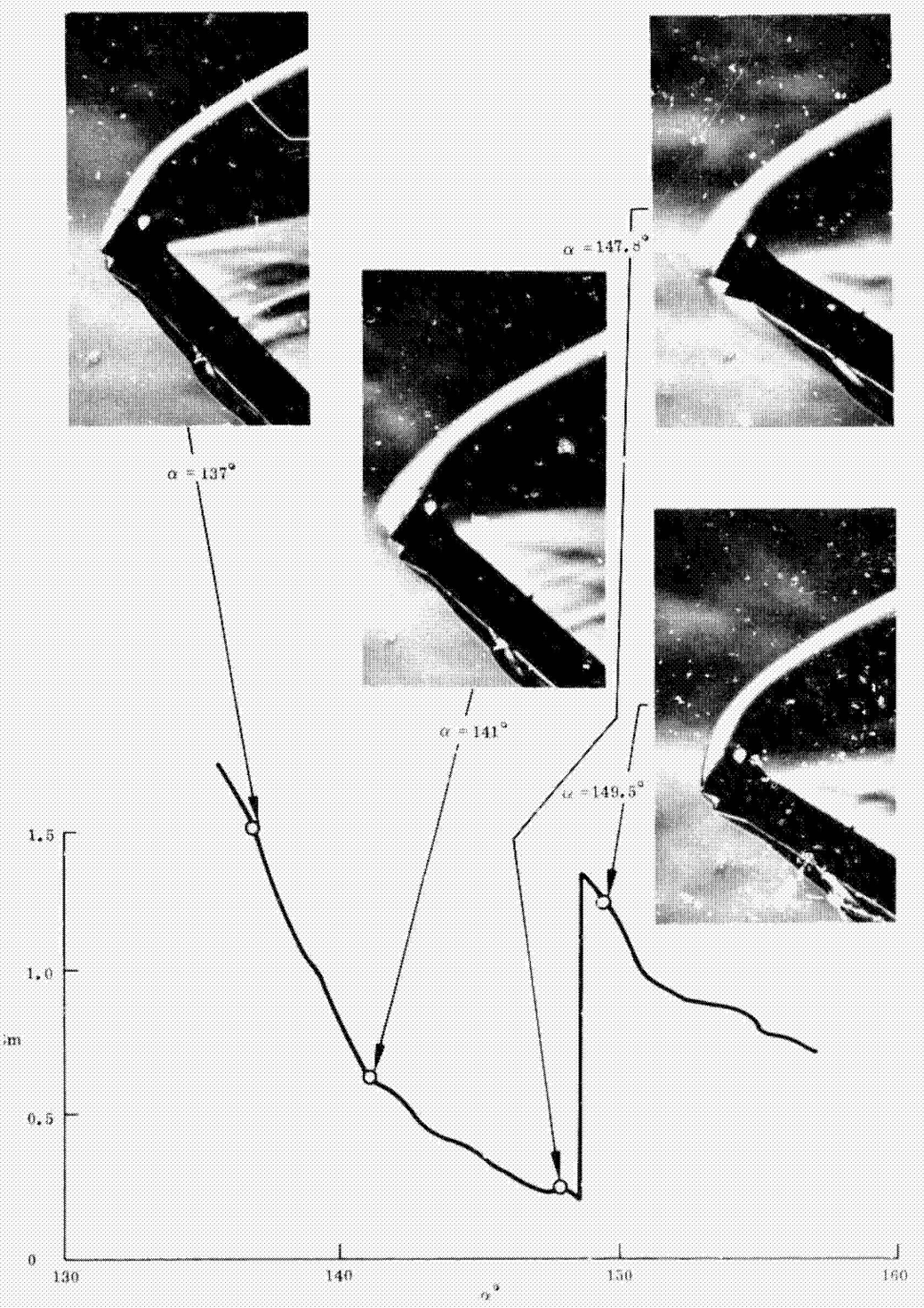

Figure 2 Shadowgraphs of SRM Flow Field at $M_\infty = 3.48$ and $140° < \alpha < 180°$

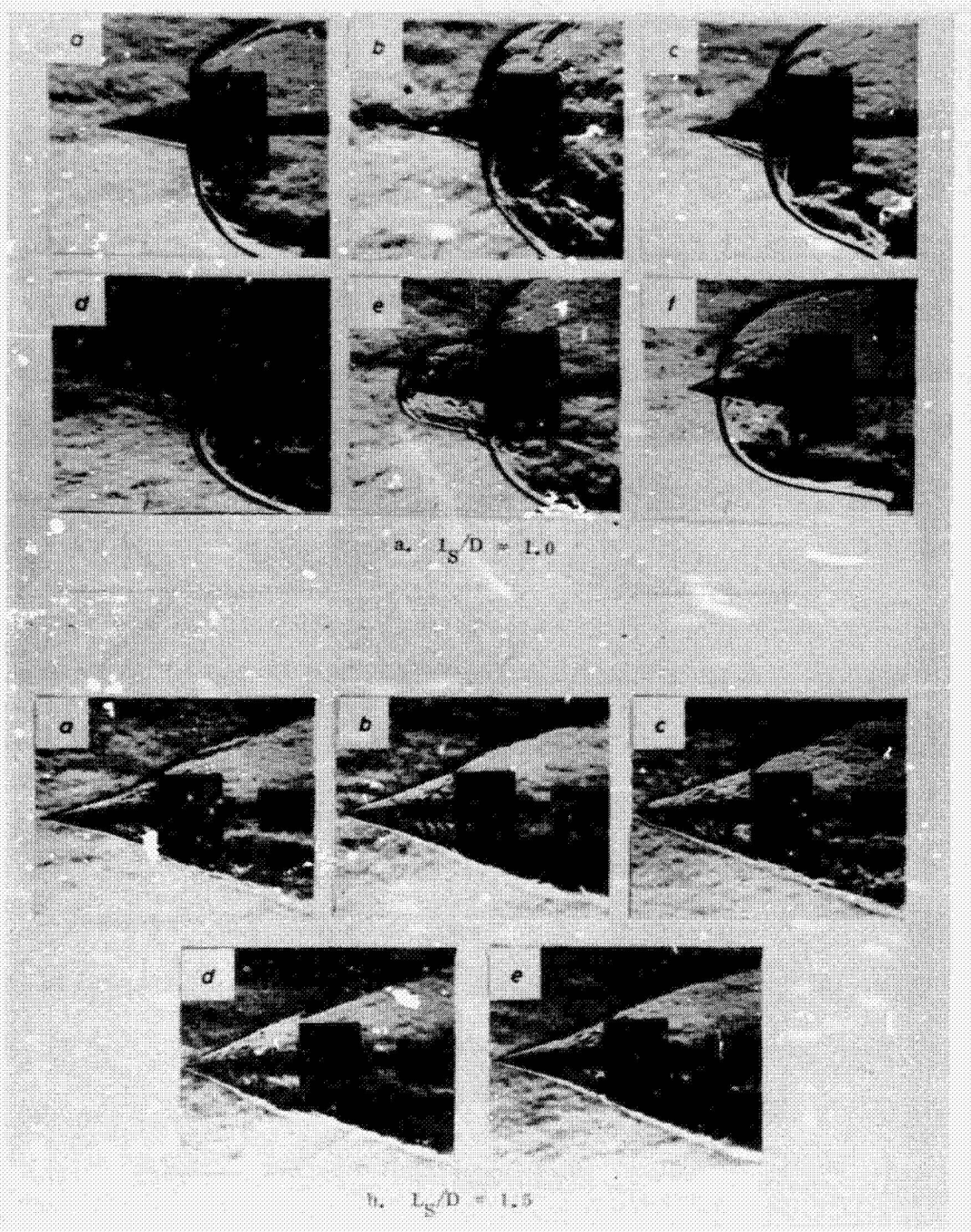

Figure 3 Shadowgraphs of Spiked Body Flow Fields at $M_\infty = 8.75$ and $\alpha = 0$

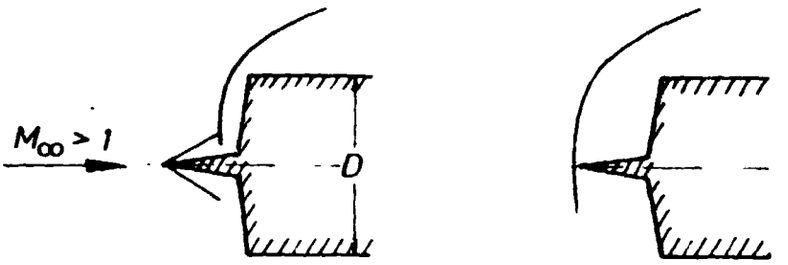

PULSATION

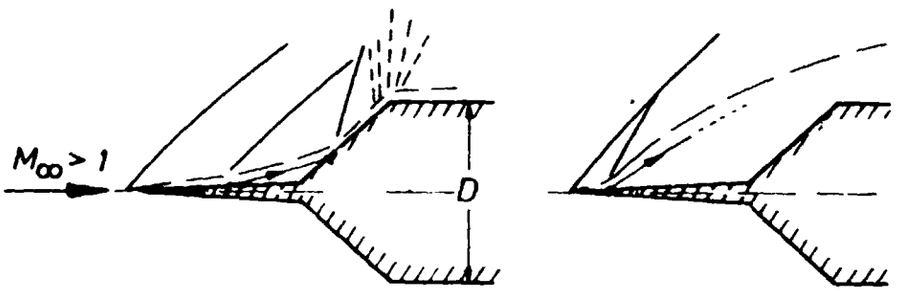

OSCILLATION

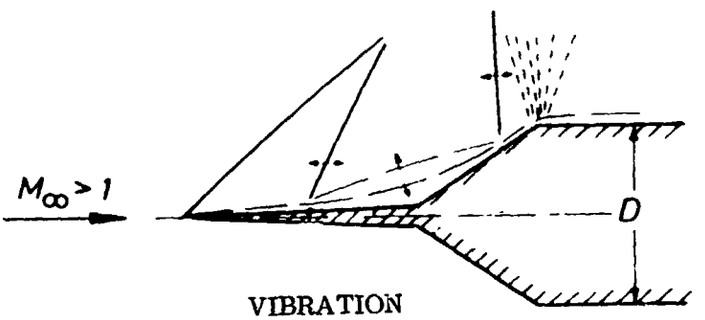

VIBRATION

Figure 4 Classification of Spiked Body Unsteady Flow Fields

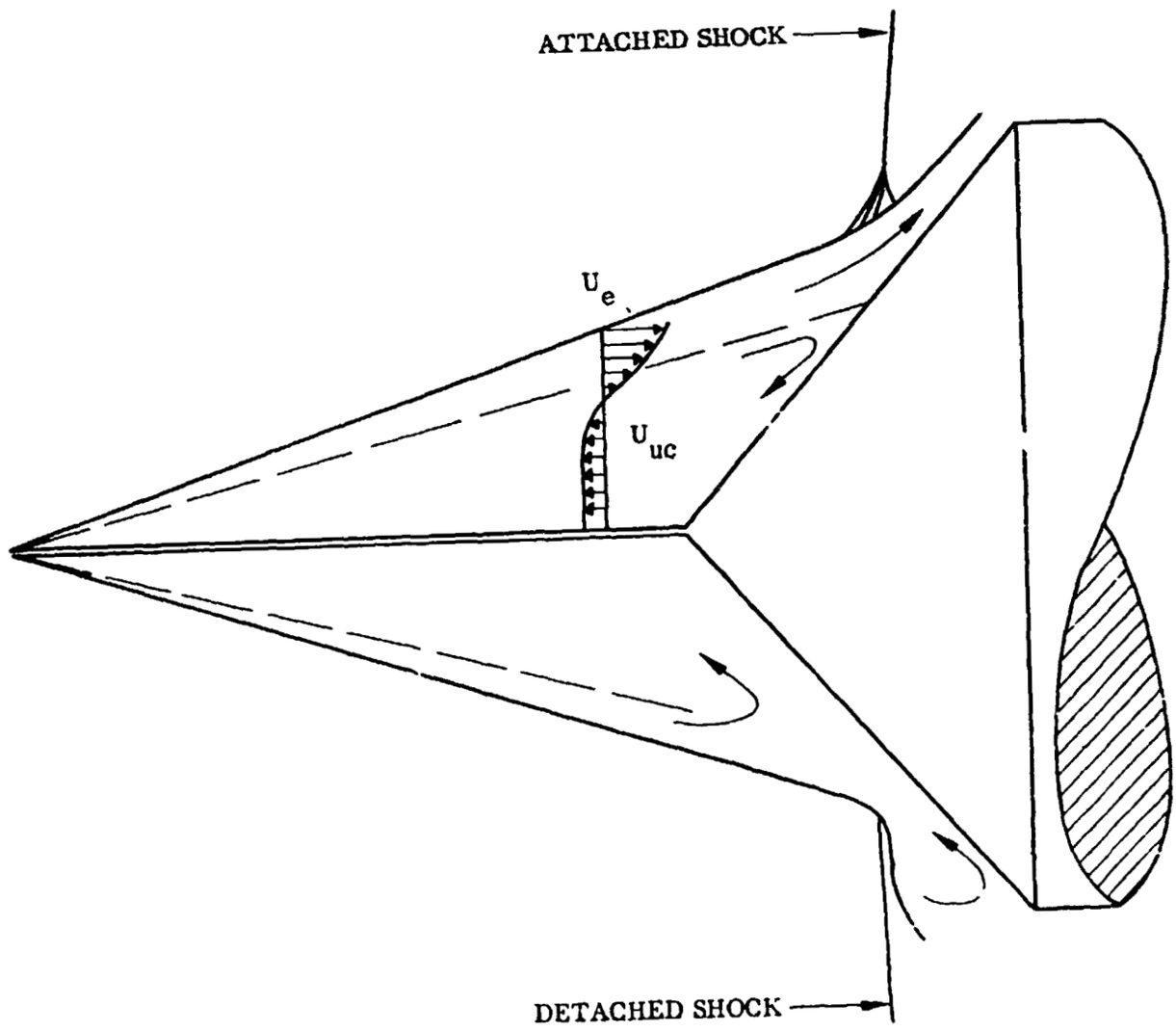

Figure 5 Stable and Unstable Spike-Induced Separated Flow

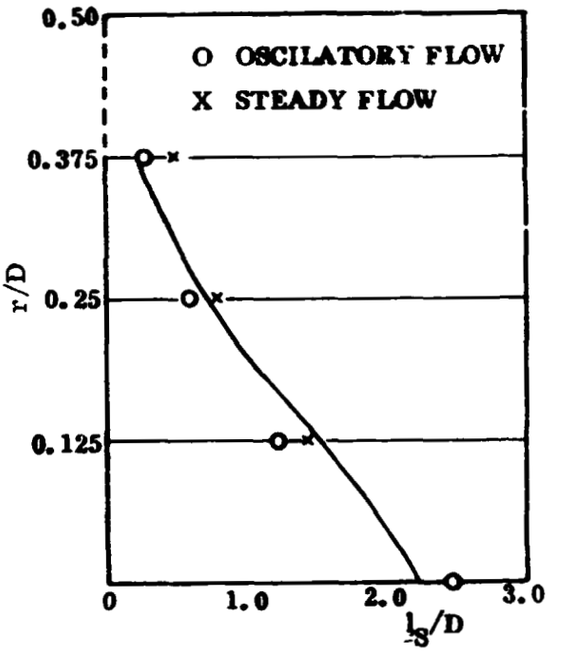

Figure 6 Critical Spiked Body Geometry

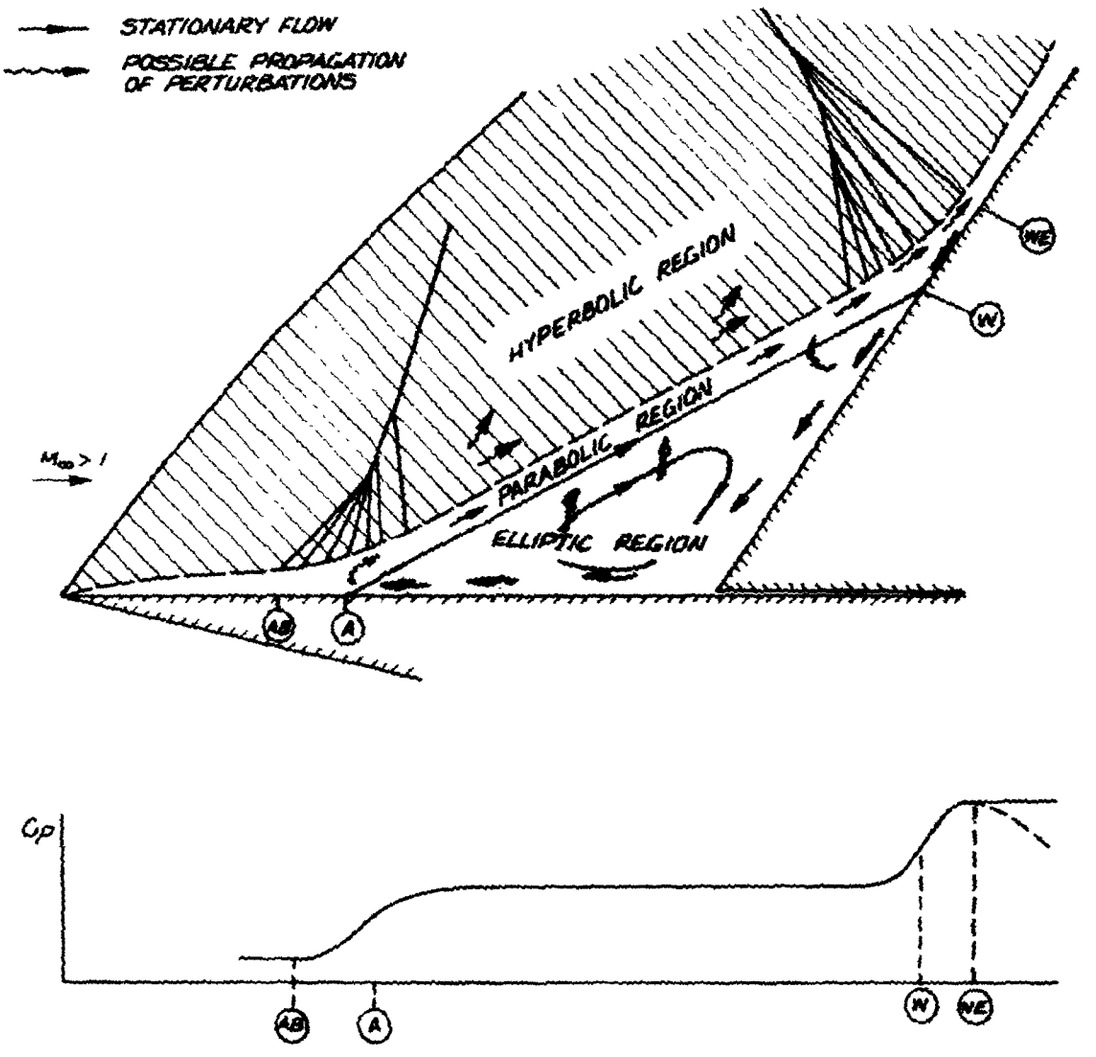

Figure 7 Definition of Flow Regions

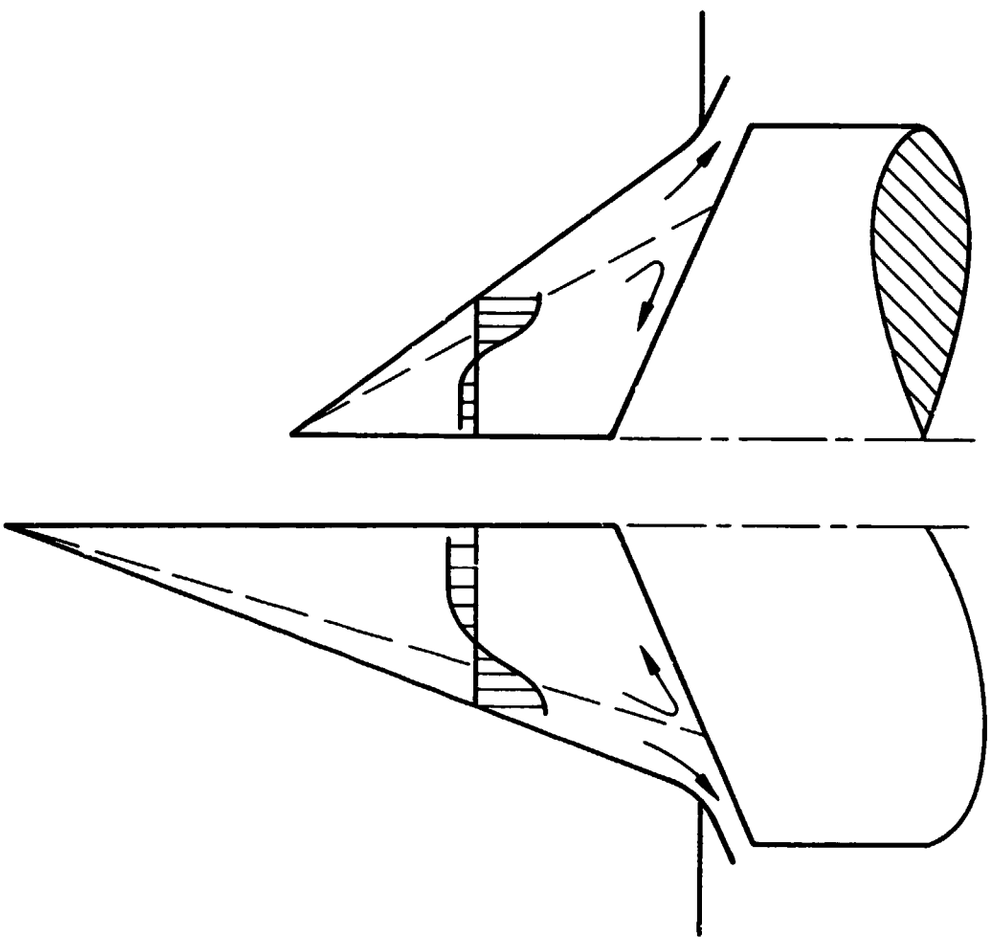

Figure 8 Effect of Spike Length

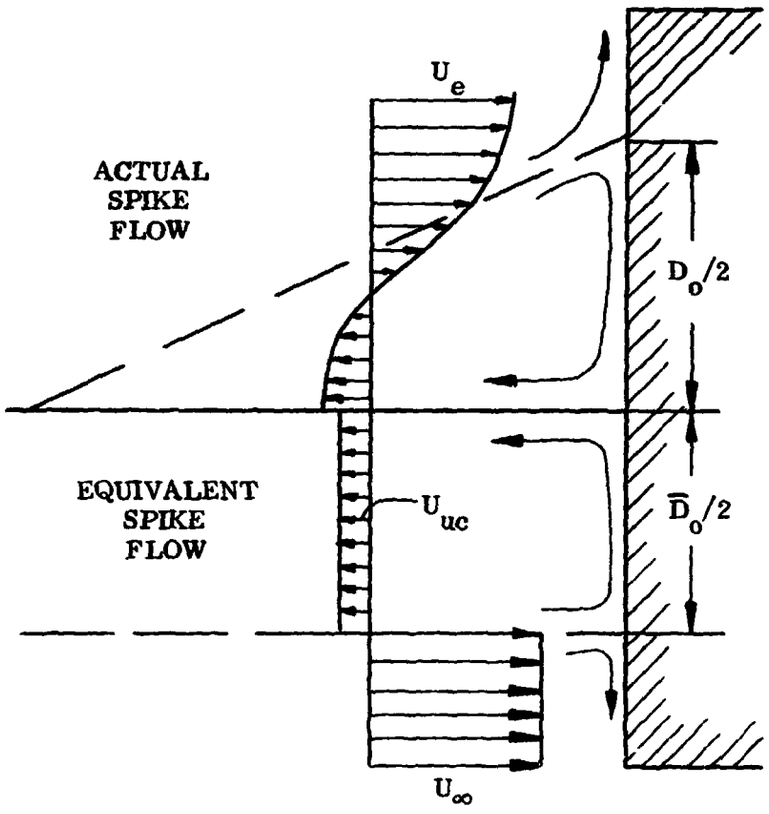

Figure 9 Idealized Separated Flow Geometry

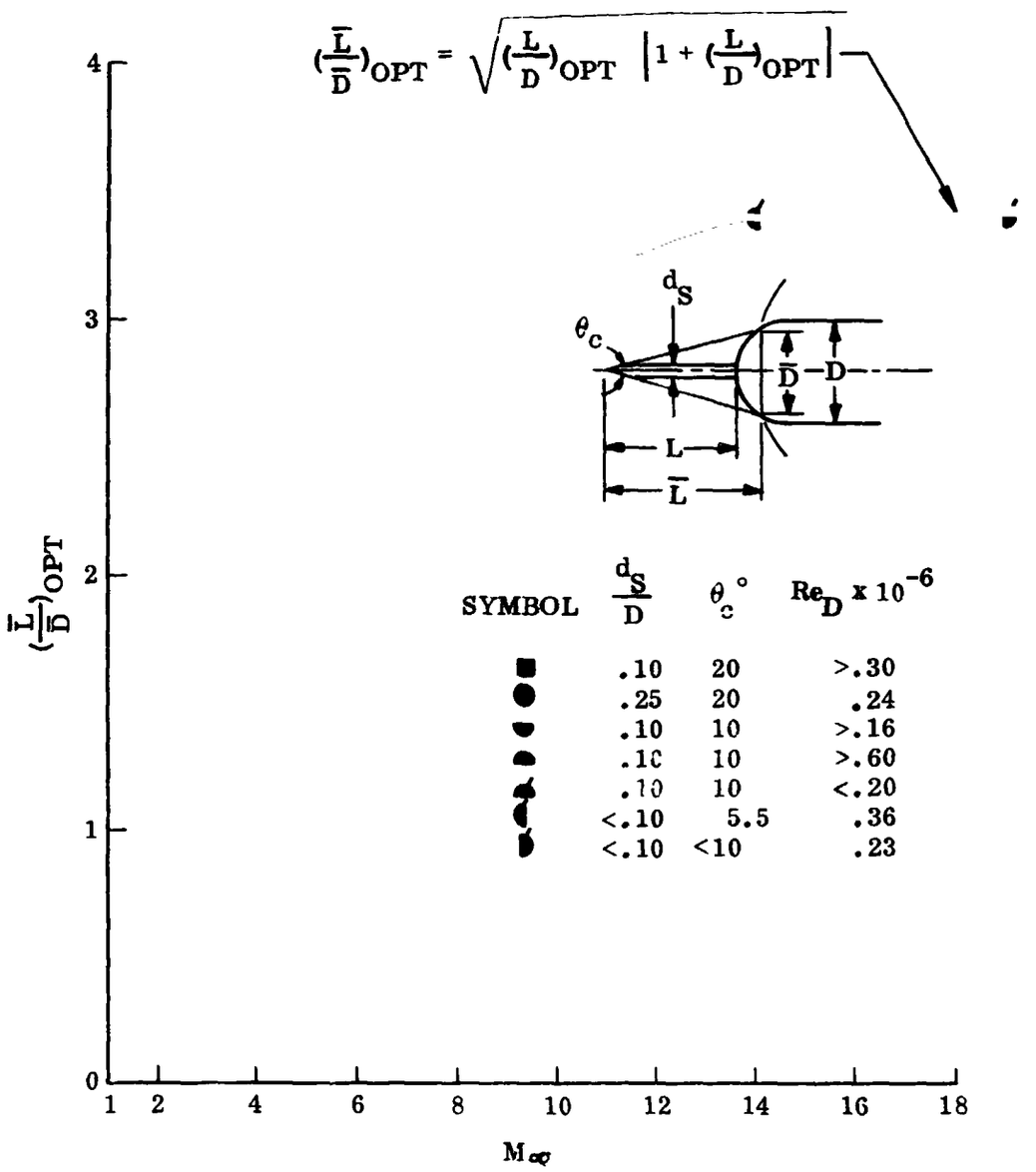

Figure 10 Optimum Spike Length as a Function of Mach Number

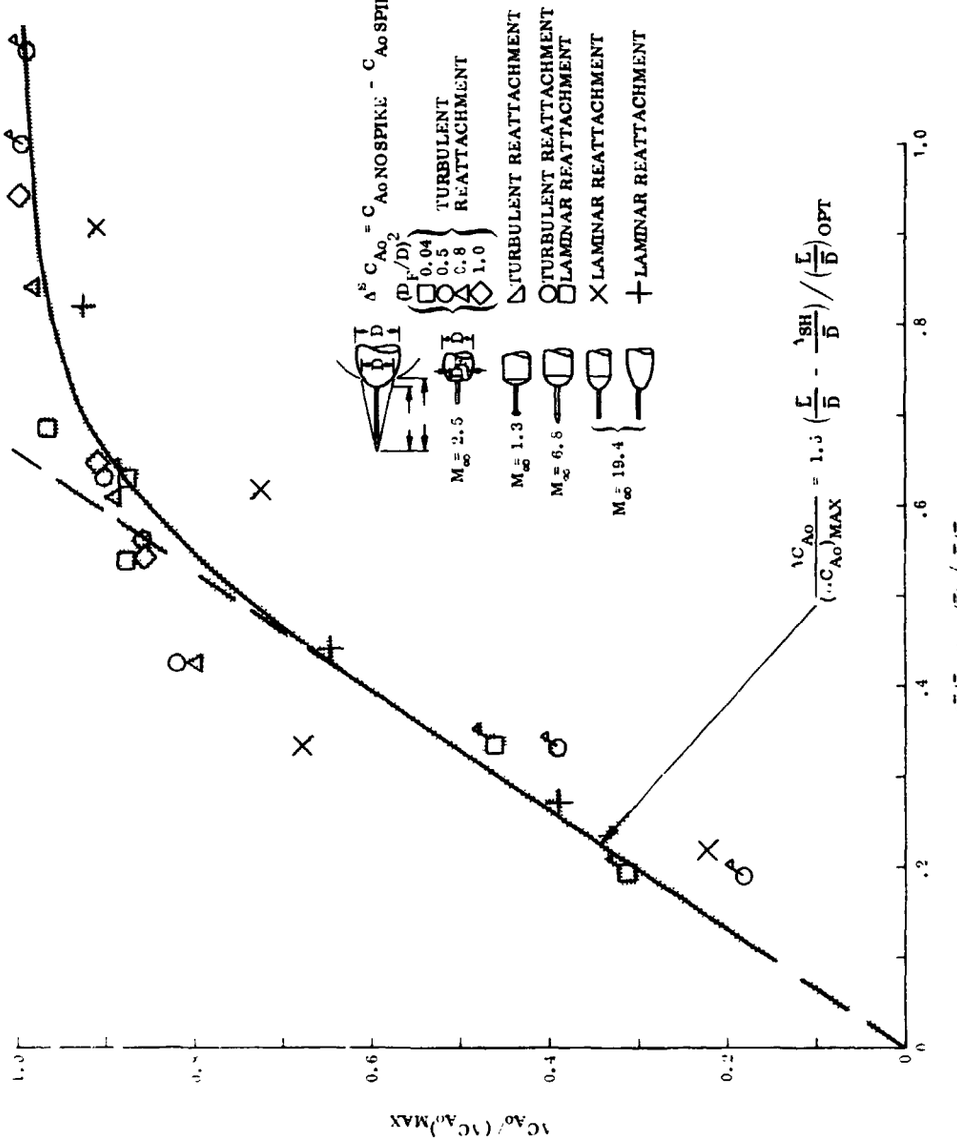

Figure 11 Spike-Induced Forebody Drag Reduction

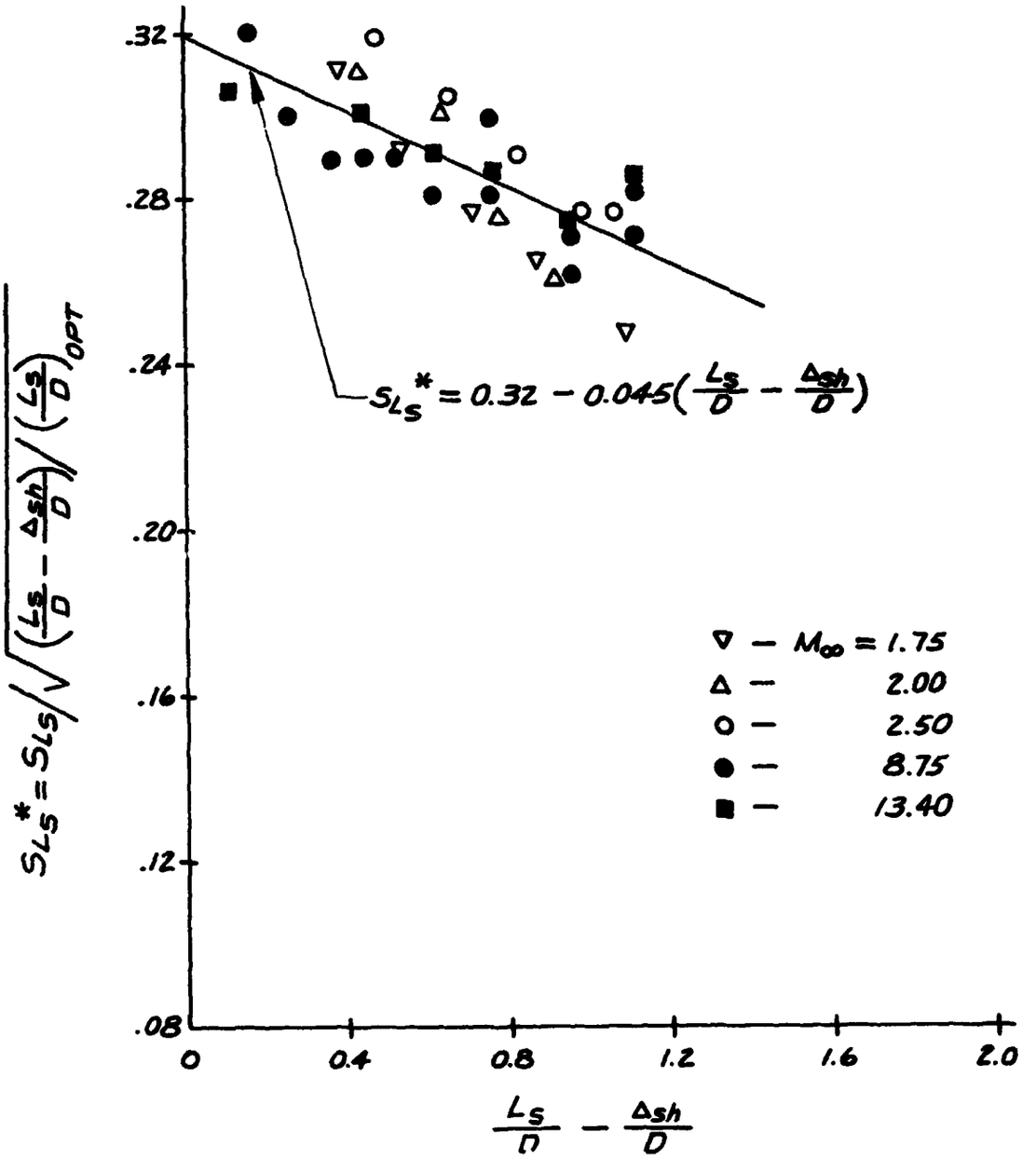

Figure 12 Normalized Strouhal Number of Spike-Induced Pulsating Flow

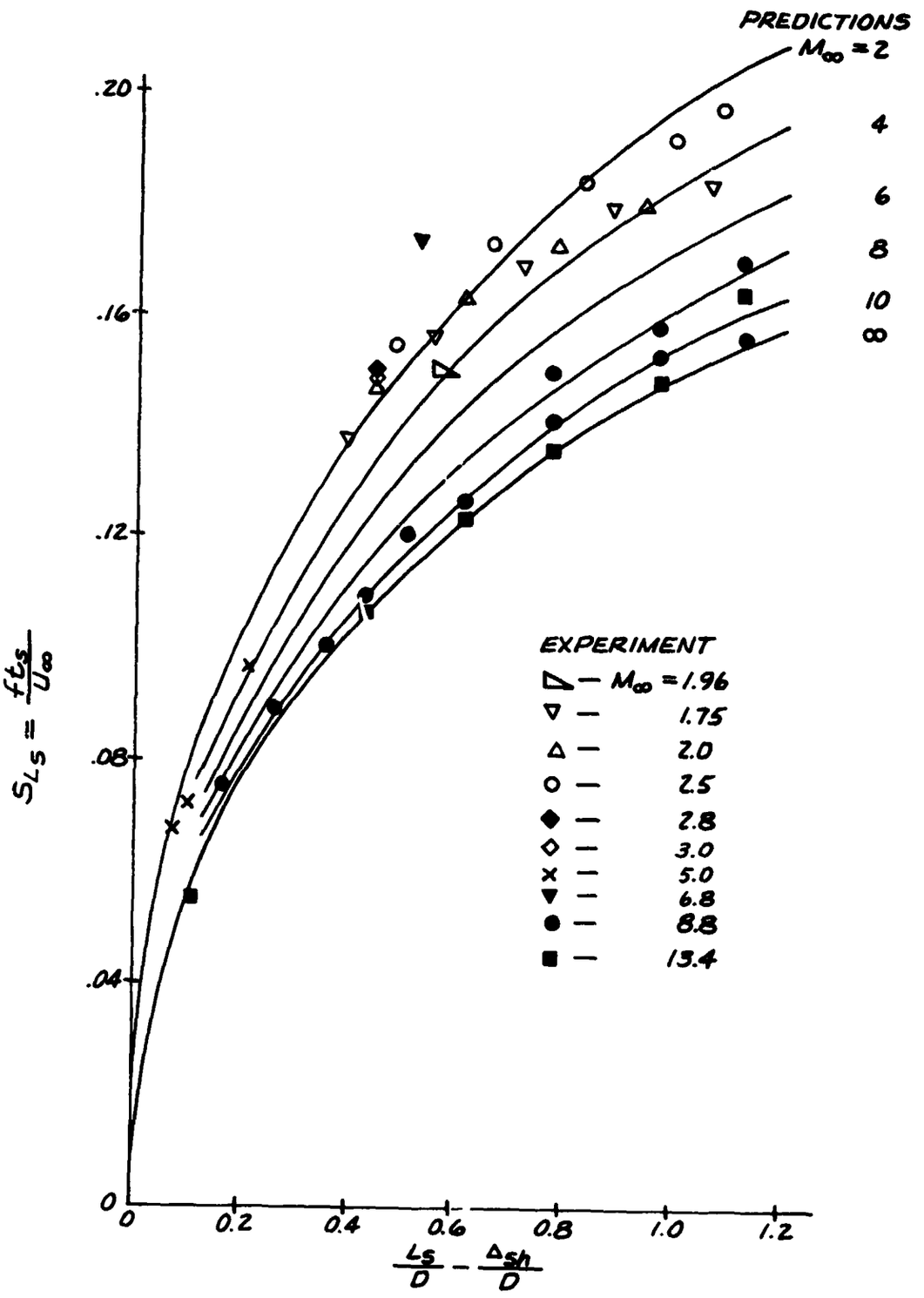

Figure 13 Predicted and Measured Frequency of Spike-Induced Pulsating Flow

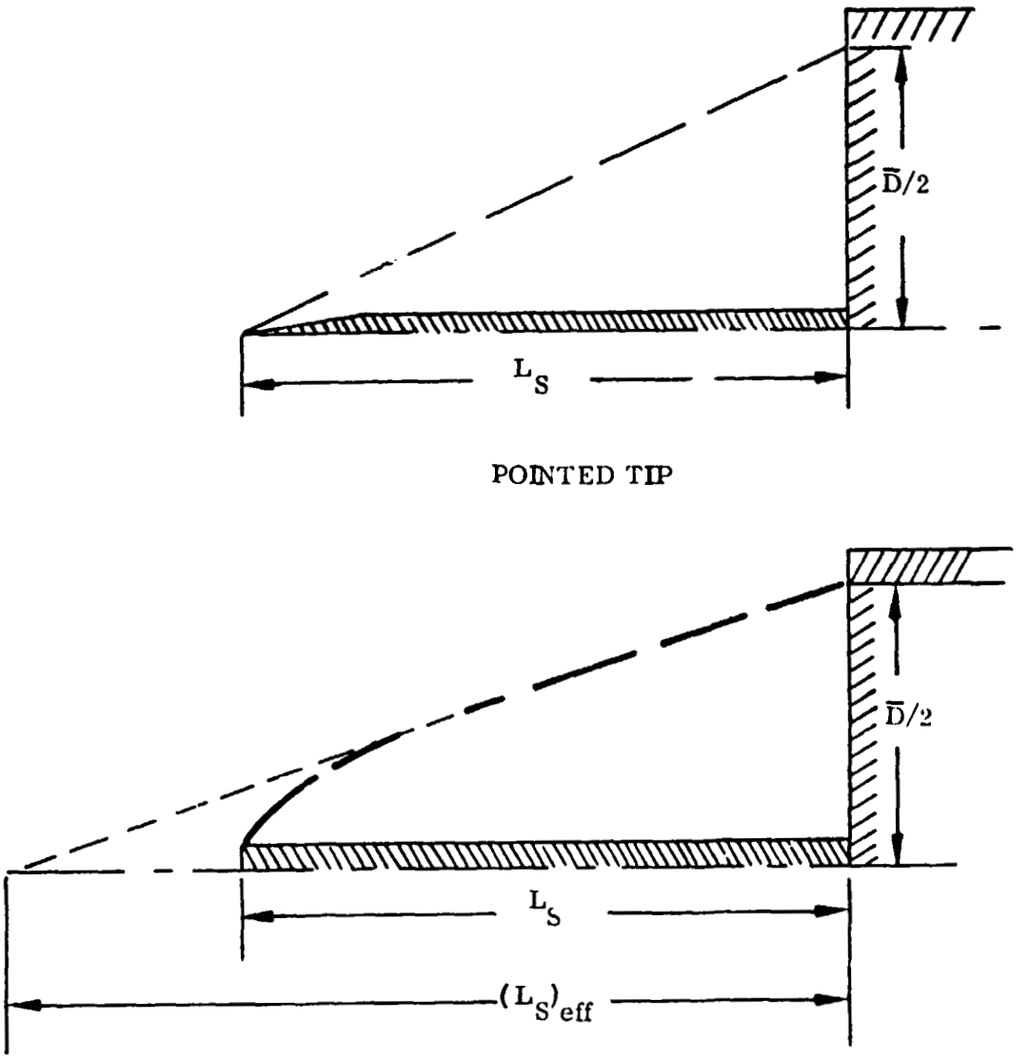

Figure 14 Conceptual Flow Geometrics for Pointed and Blunt Spikes

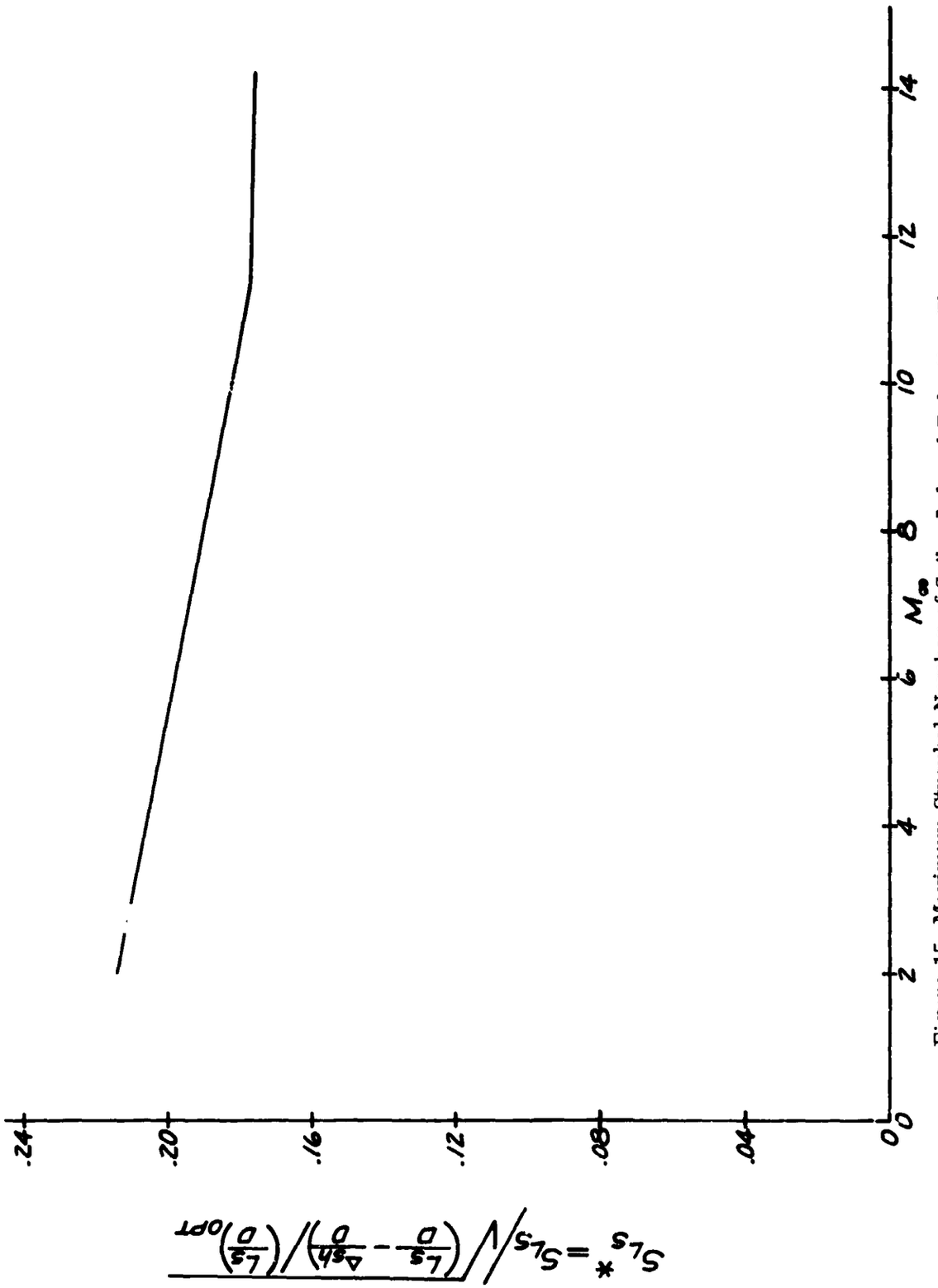

Figure 15 Maximum Strouhal Number of Spike-Induced Pulsating Flow

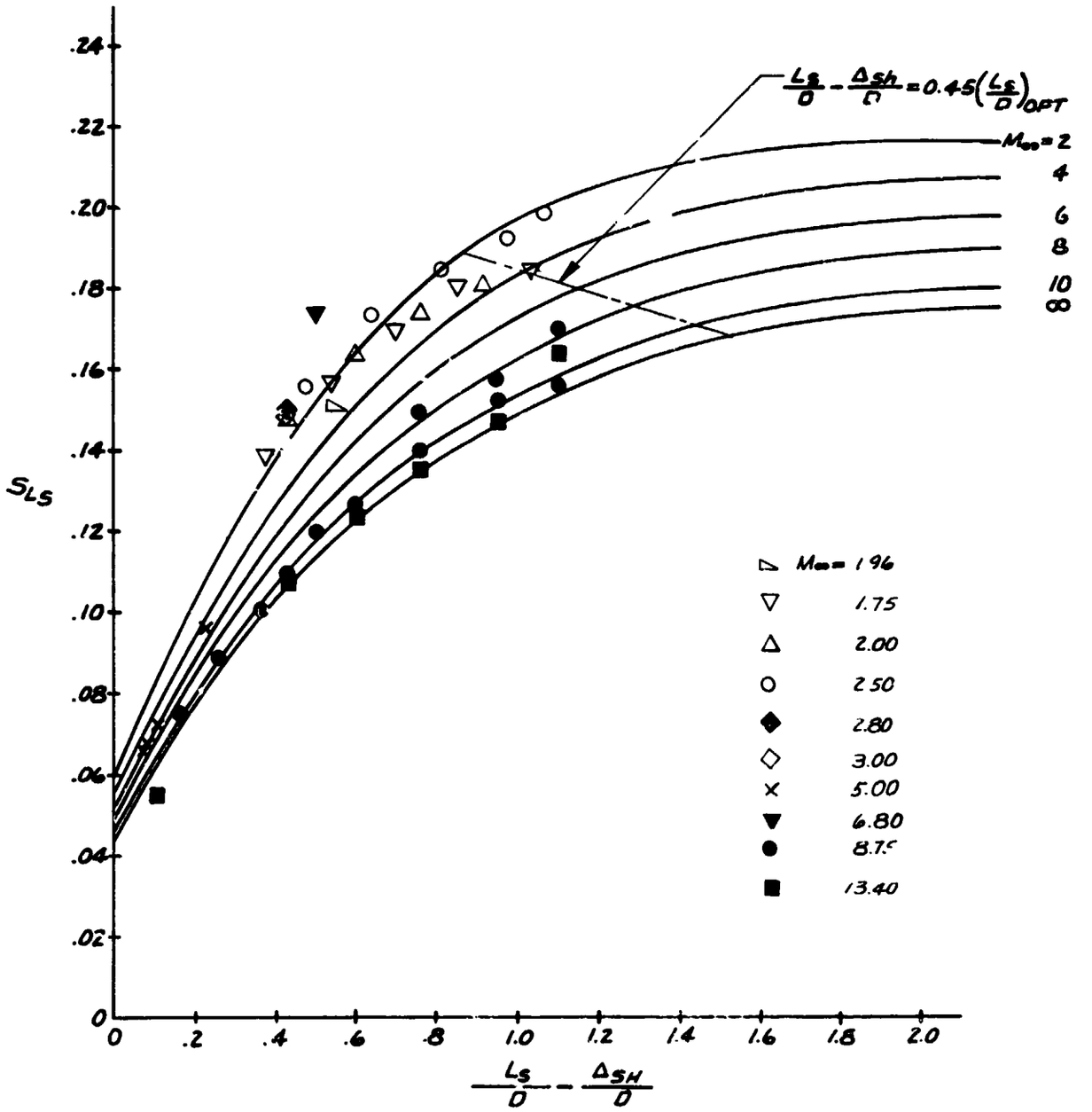

Figure 16 Comparison Between Predicted ard Measured Strouhal Numbers of Spike-Induced Flow Pulsations

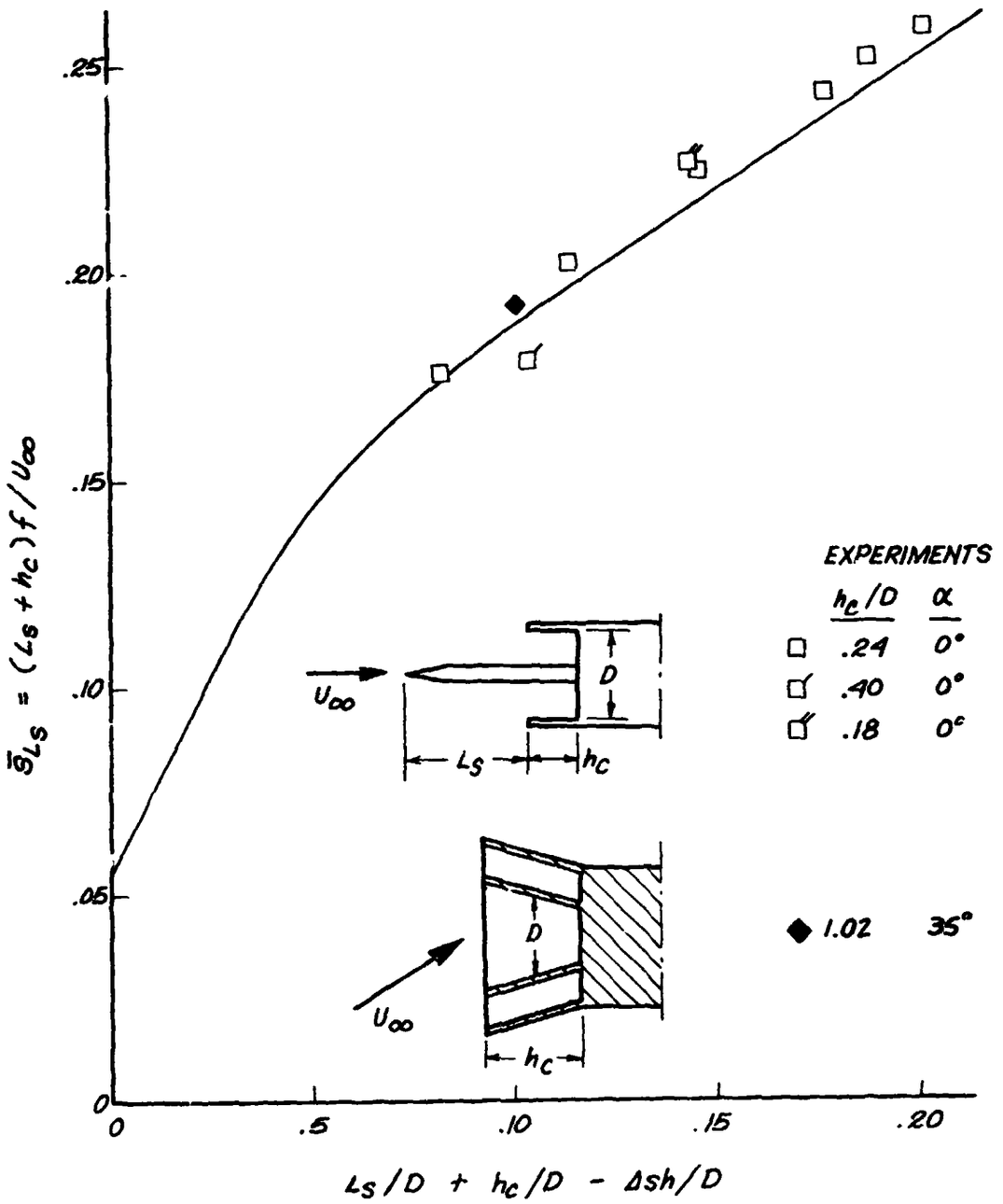

Figure 17 Predicted and Measured Frequency of Pulsating Flow in Forward Facing Cavities at $M_\infty = 3.5$

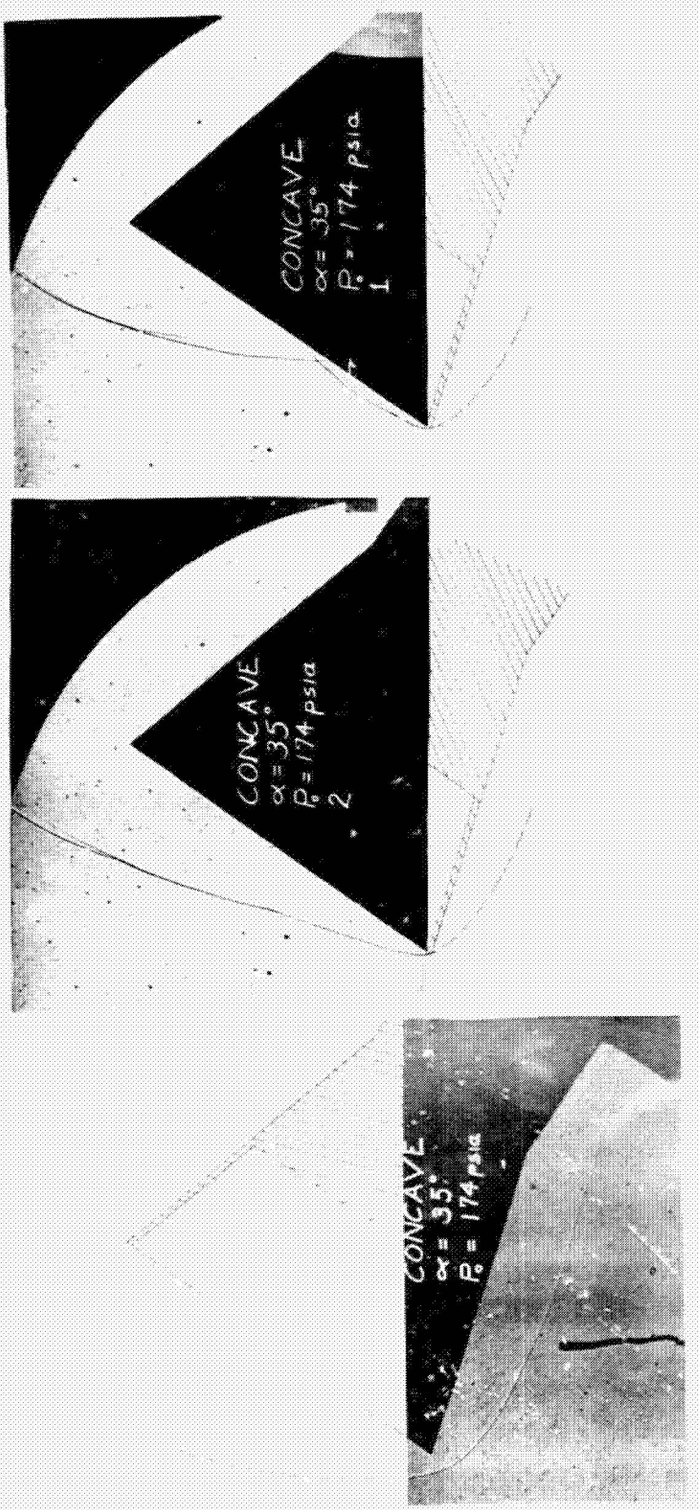

Figure 18 Shadowgraphs of Flow Over Forward Facing Cavity at 35 Degrees Flow Inclination

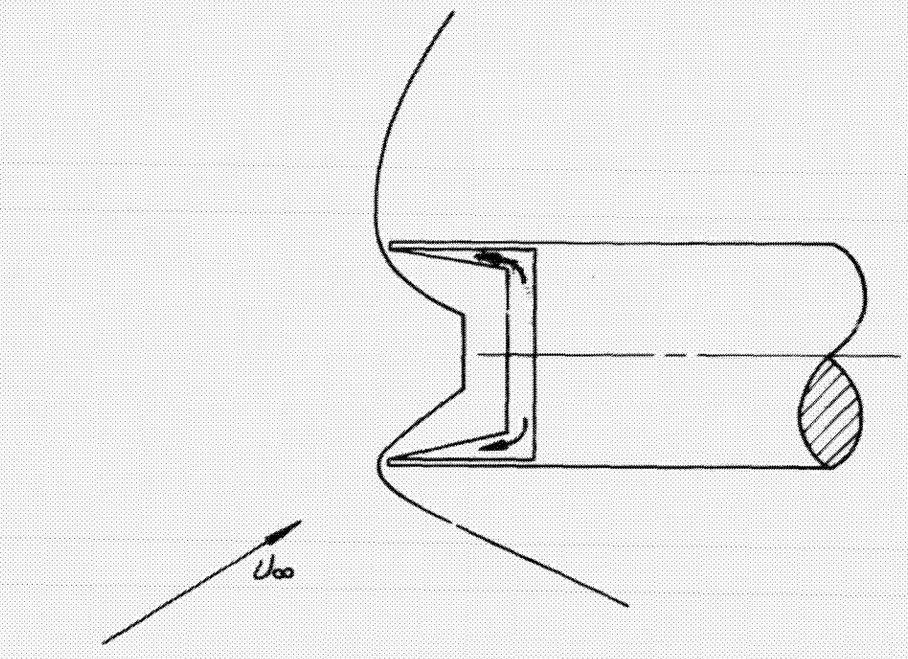

a. CAVITY ALONE AT $\alpha \neq 0$

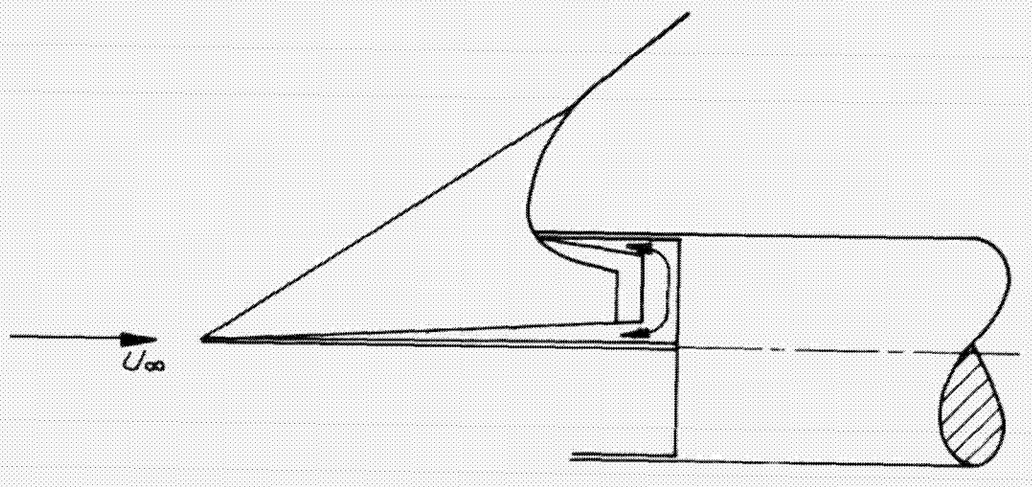

b. SPIKED CAVITY AT $\alpha = 0$

Figure 19 Conceptual Cavity Flow Fields

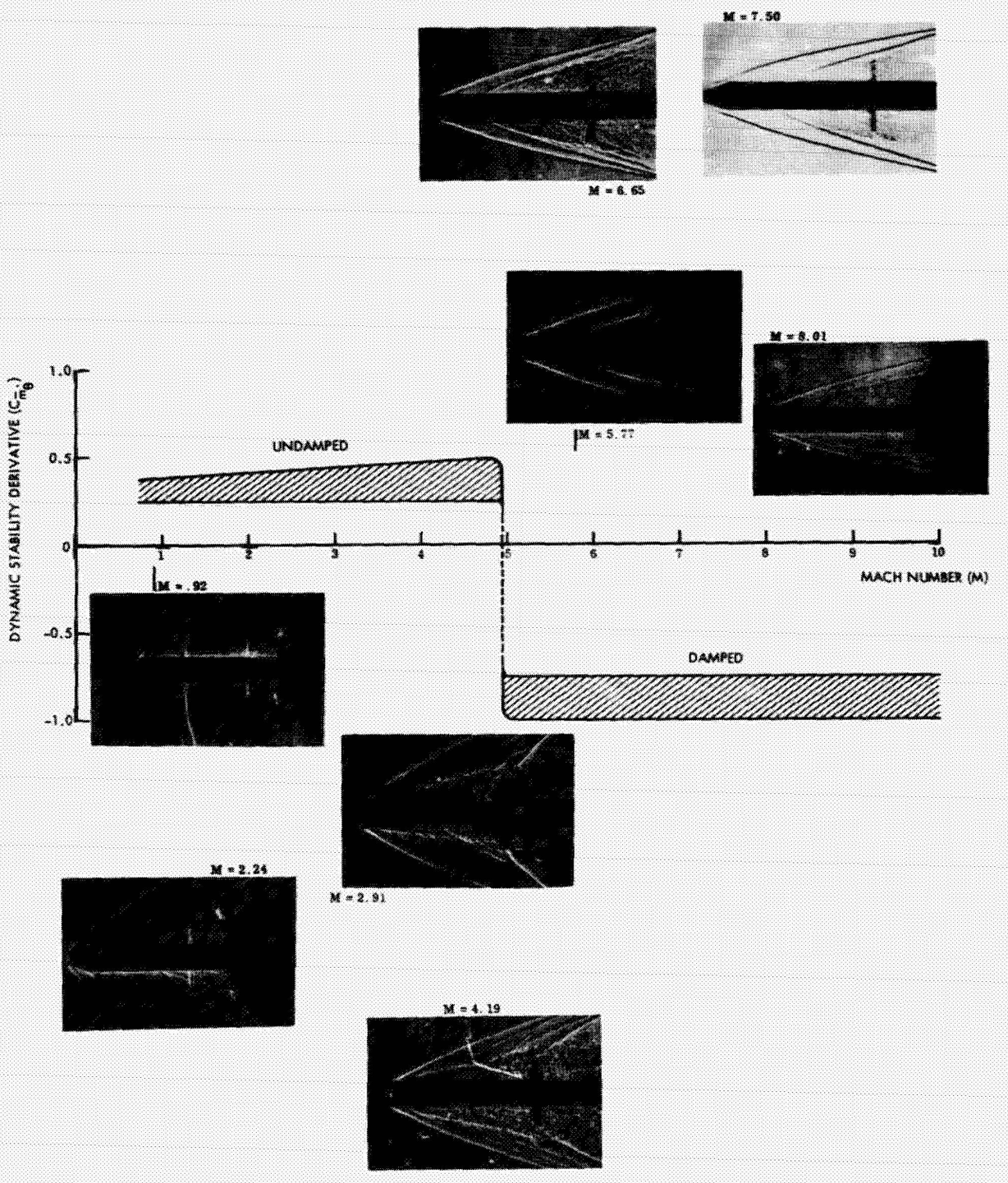

Figure 20 Effect of Mach Number on Disk-Induced Flow Separation and Associated Aerodynamic Damping in Pitch

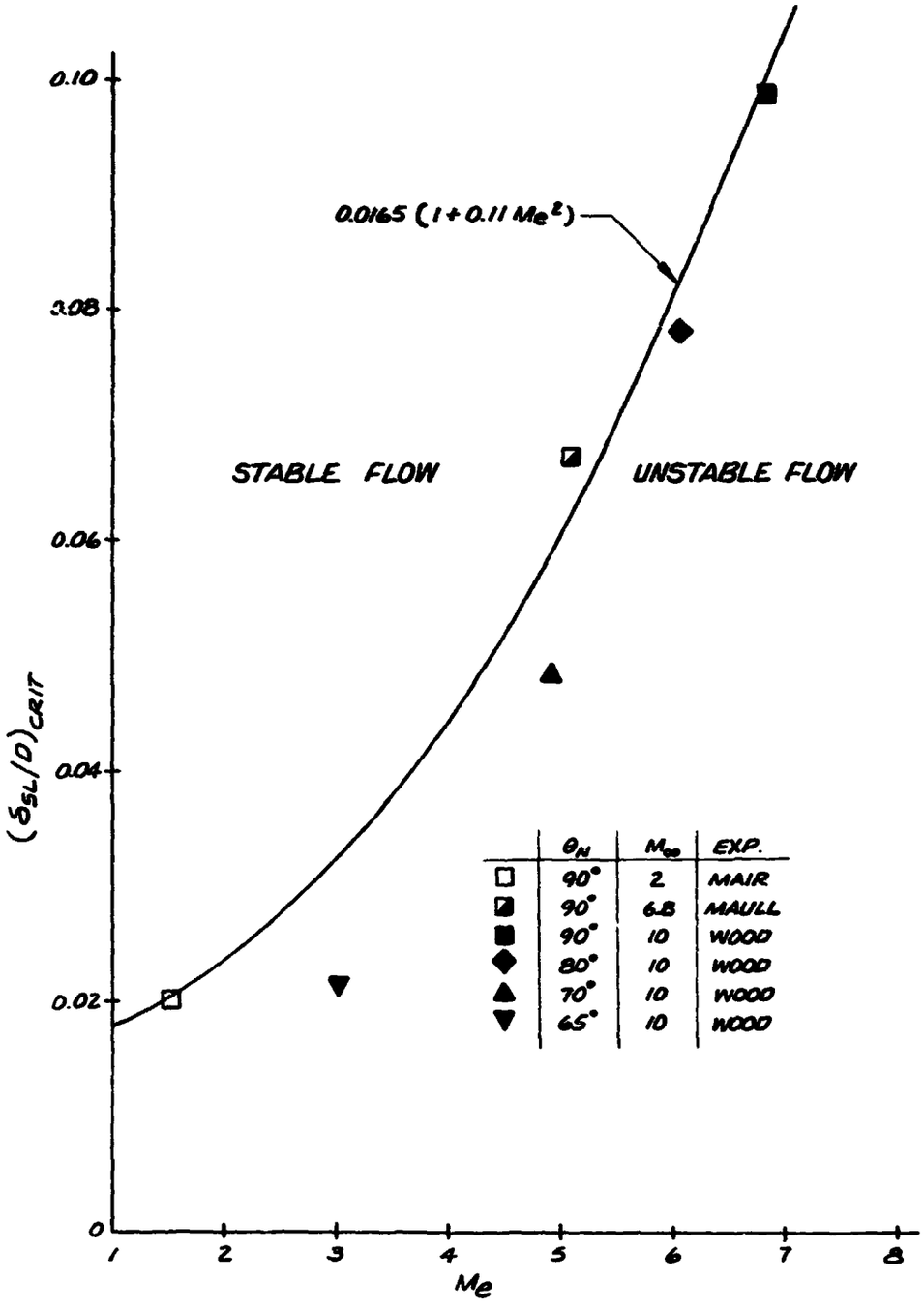

Figure 21 Critical Shear Layer Thickness for Incipient Flow Pulsations

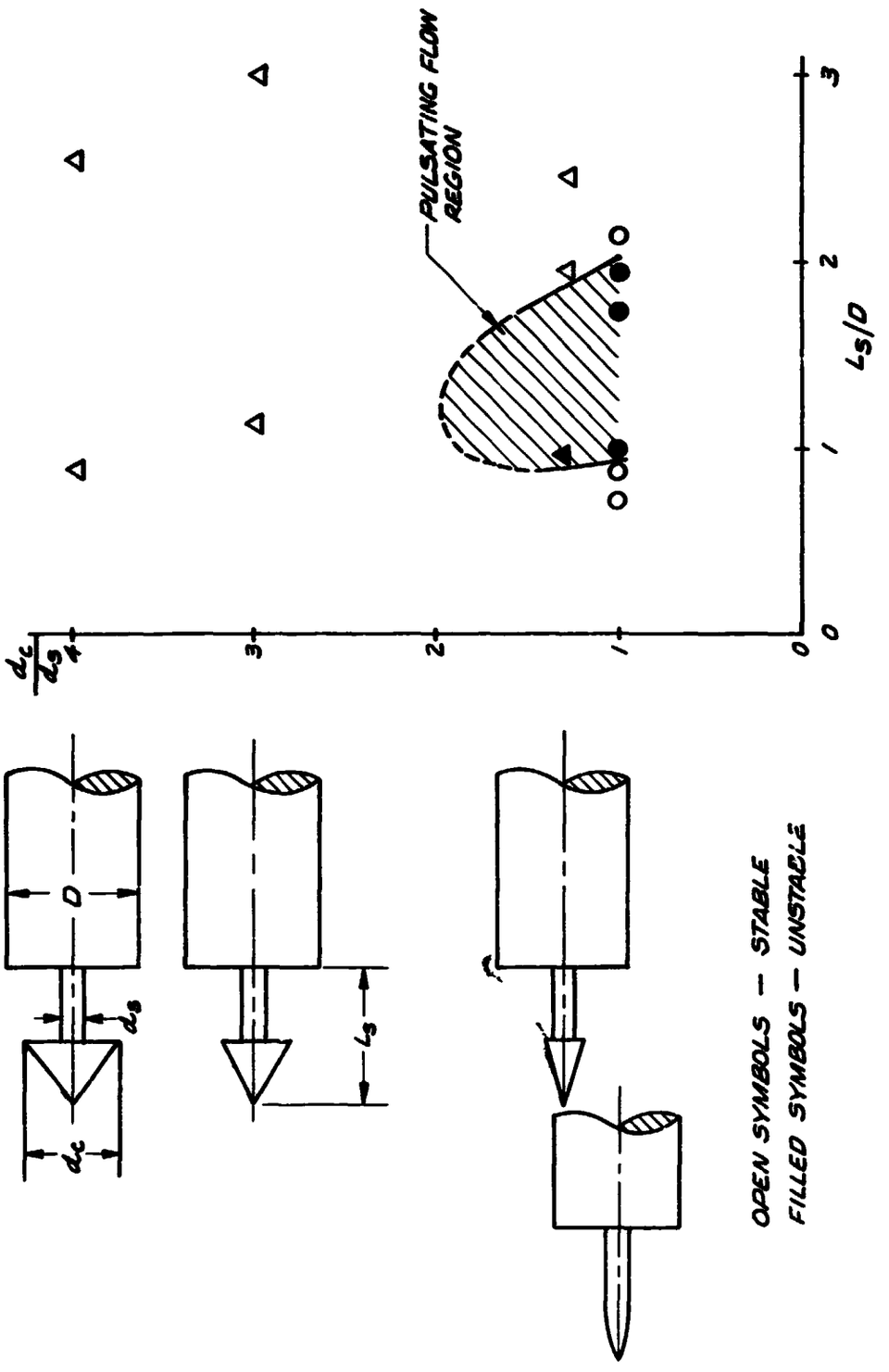

Figure 22 Effect of Spike-Hammerheads on Spike-Induced Flow Pulsations

(c) Steady flow; $\alpha \approx 0^{o}$.

(d) Steady flow; $\alpha \approx 2^{o}$

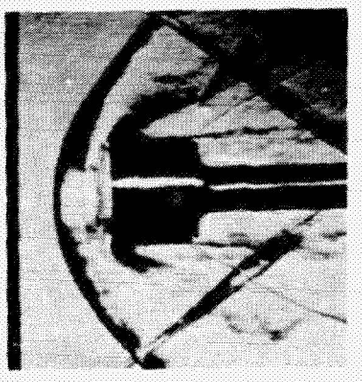

(e) Unsteady flow; $\alpha \approx 0^{o}$.

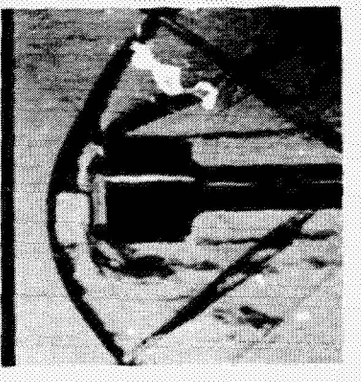

(f) Unsteady flow; $\alpha \approx 0^{o}$.

Figure 23 Pseudo-Stable Flow Configurations for Forward Facing Hemispherical Cavity

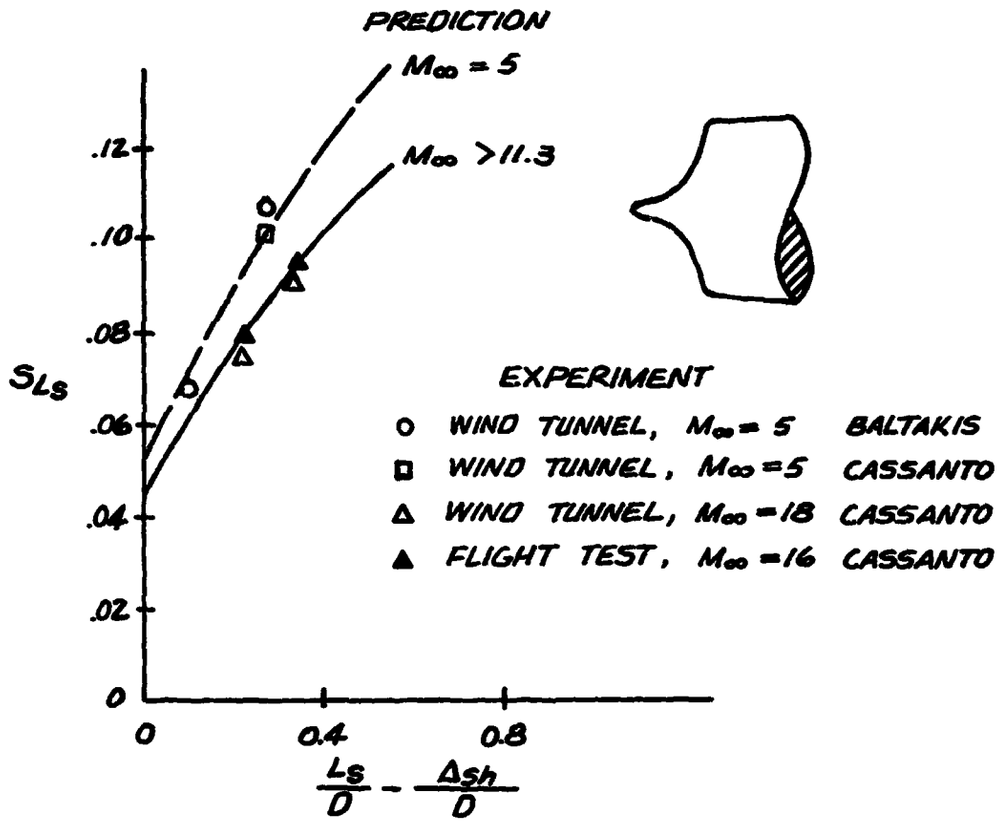

Figure 24 Flow Pulsations on Probescidean Nose Geometries

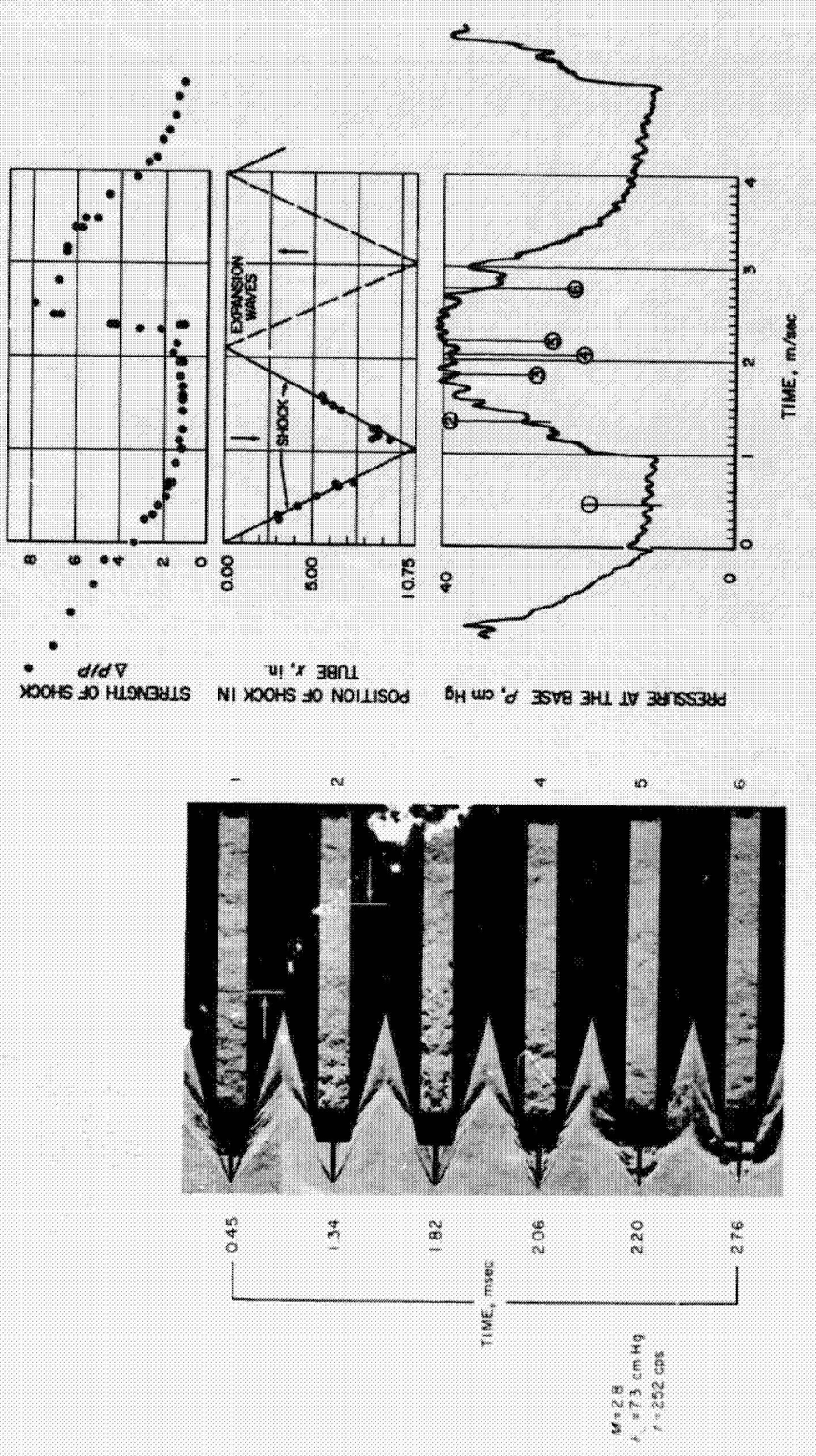

Figure 25 Characteristics of Unsteady Flow in a Resonance Tube with Flow Separation Spike

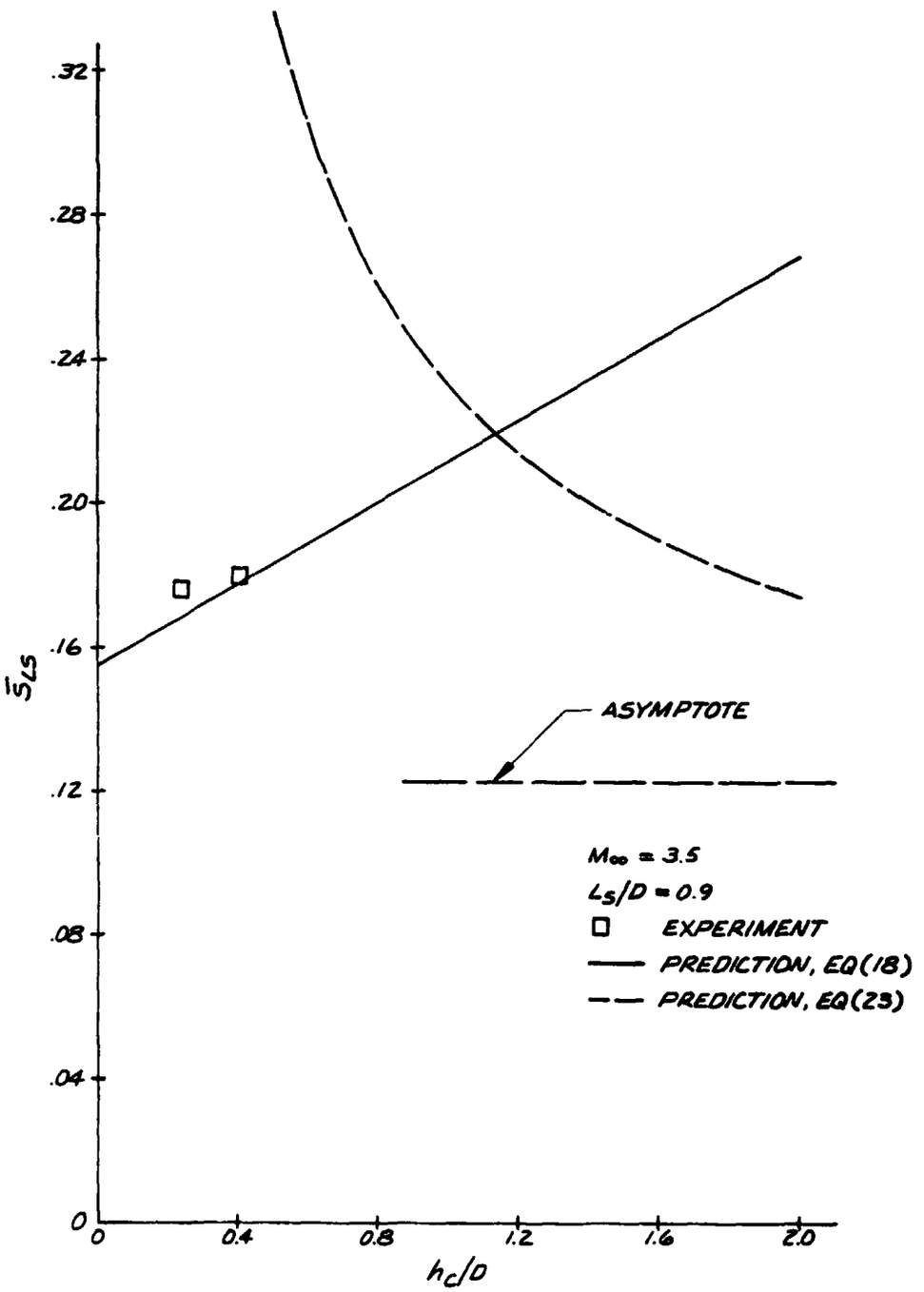

Figure 26 Effect of Cavity Depth on Oscillation Frequency

Figure 27 Shadowgraph of Flow Over Space Shuttle Launch Configuration at $M_\infty = 1.2$ and $\alpha = 0$

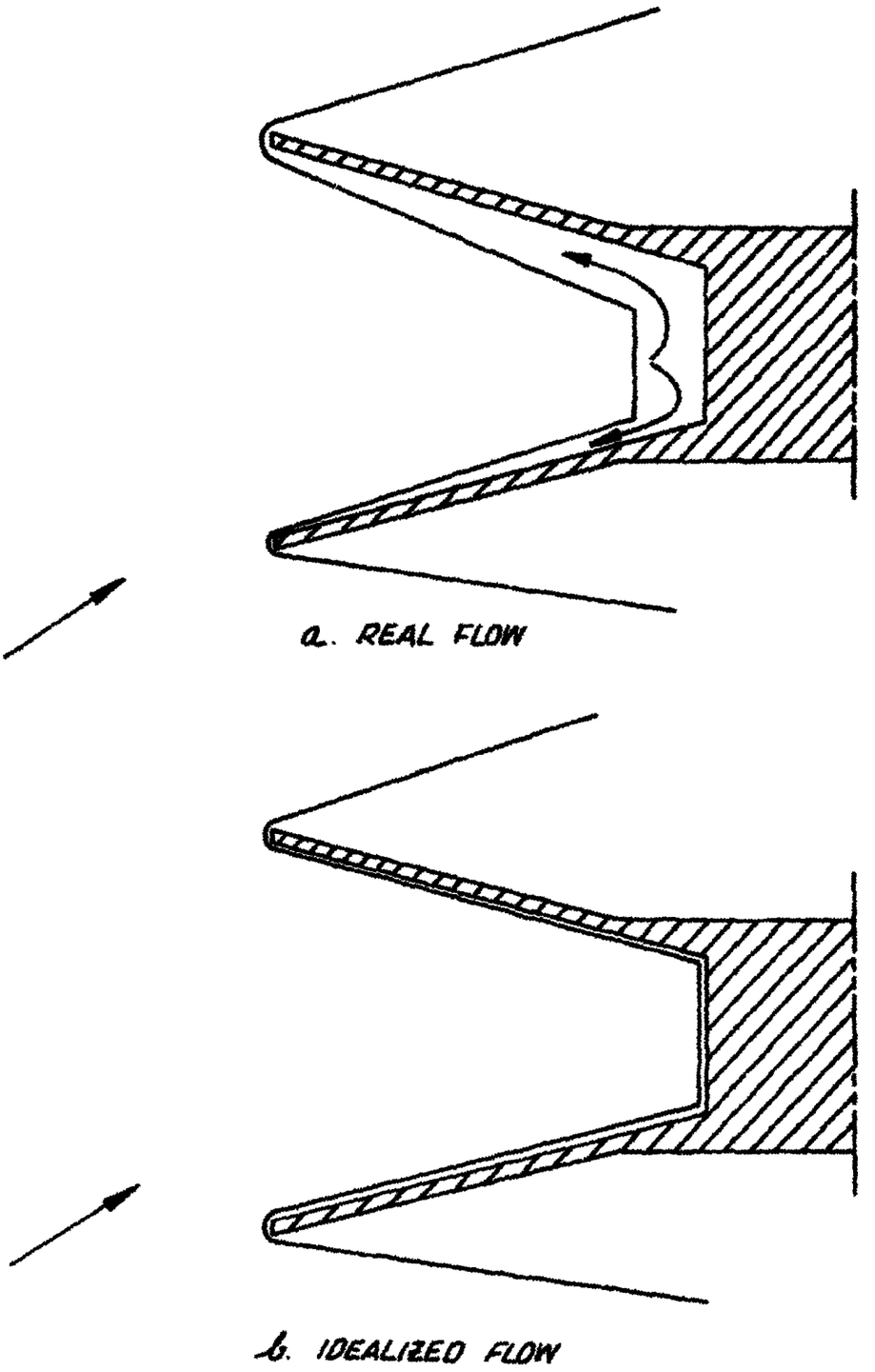

Figure 28 Idealized Moving Shock Process in the SRM Nozzles

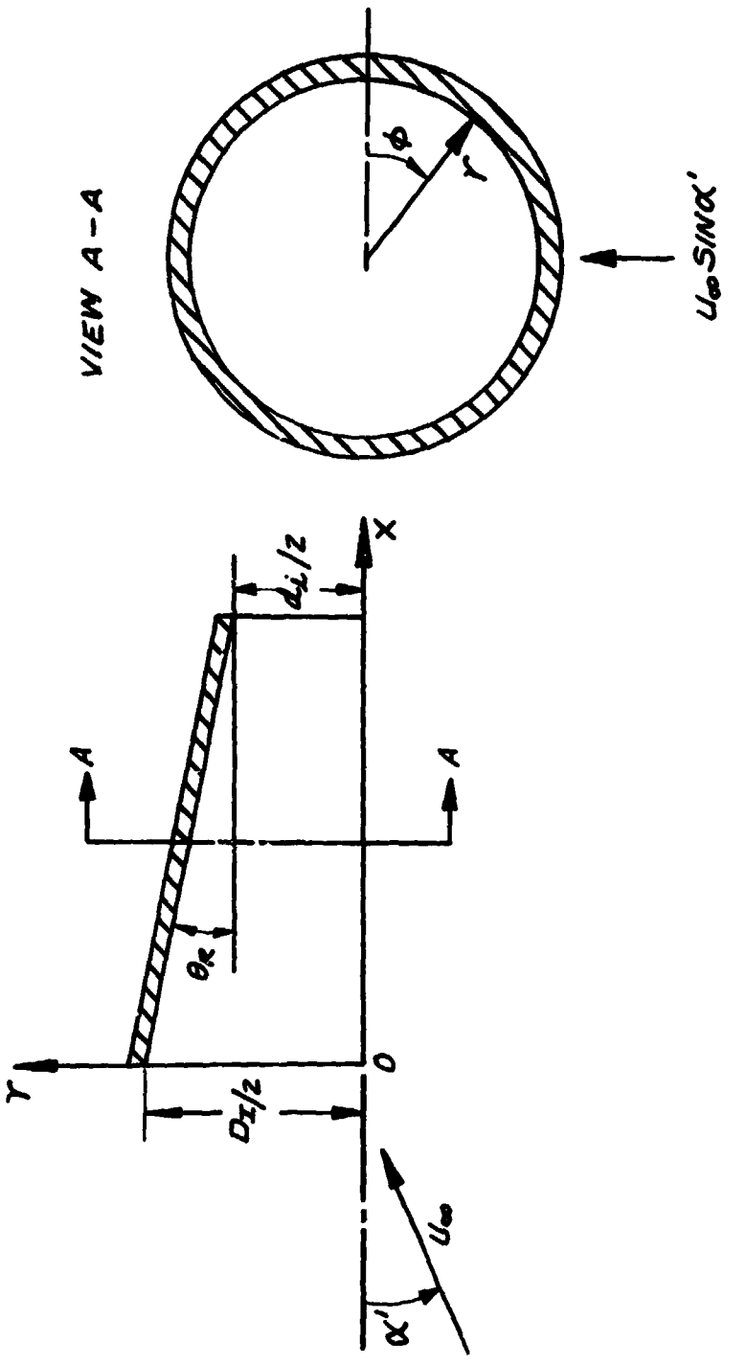

Figure 29 Definition of Nozzle Geometry

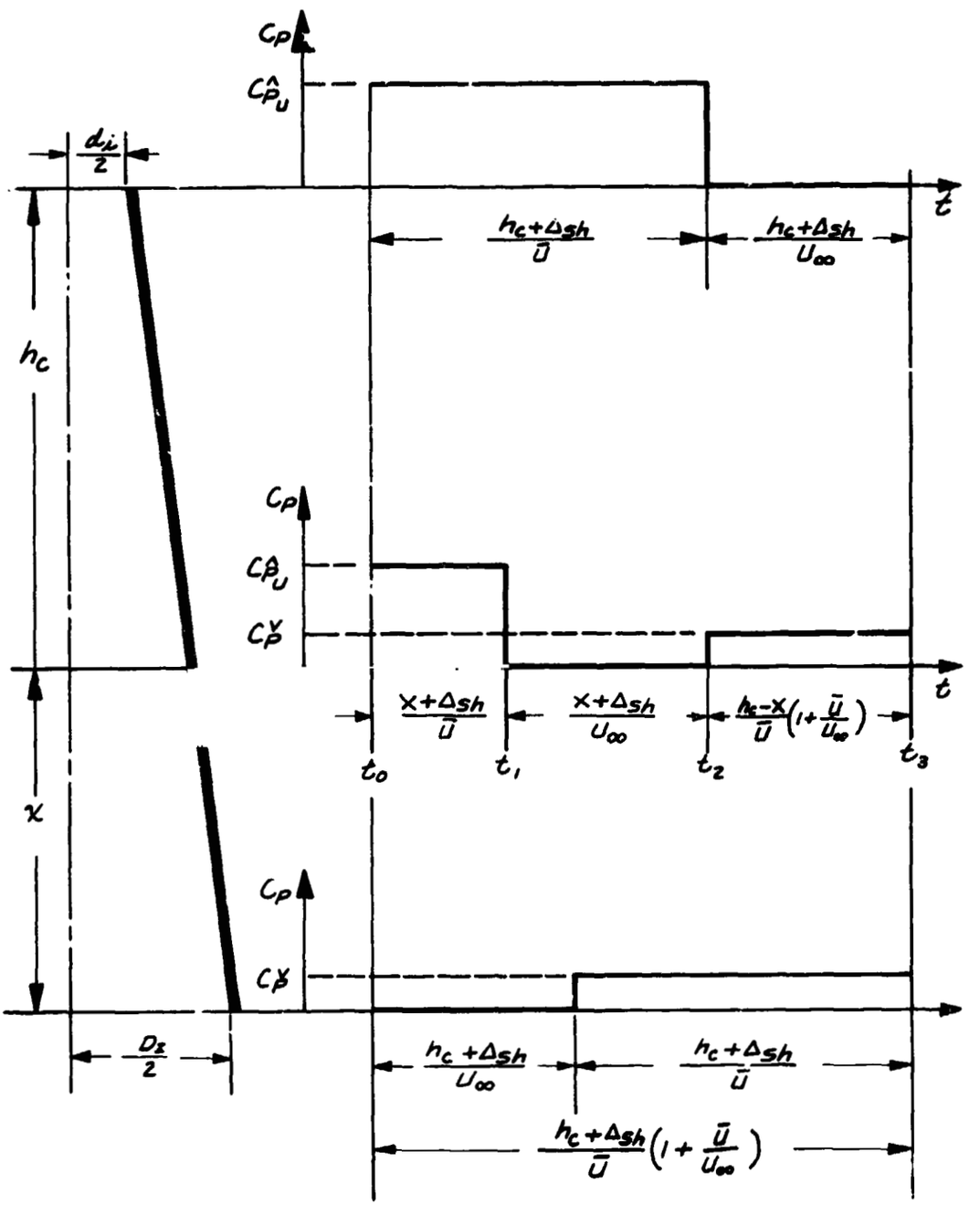

Figure 30 Idealized Pressure Time History

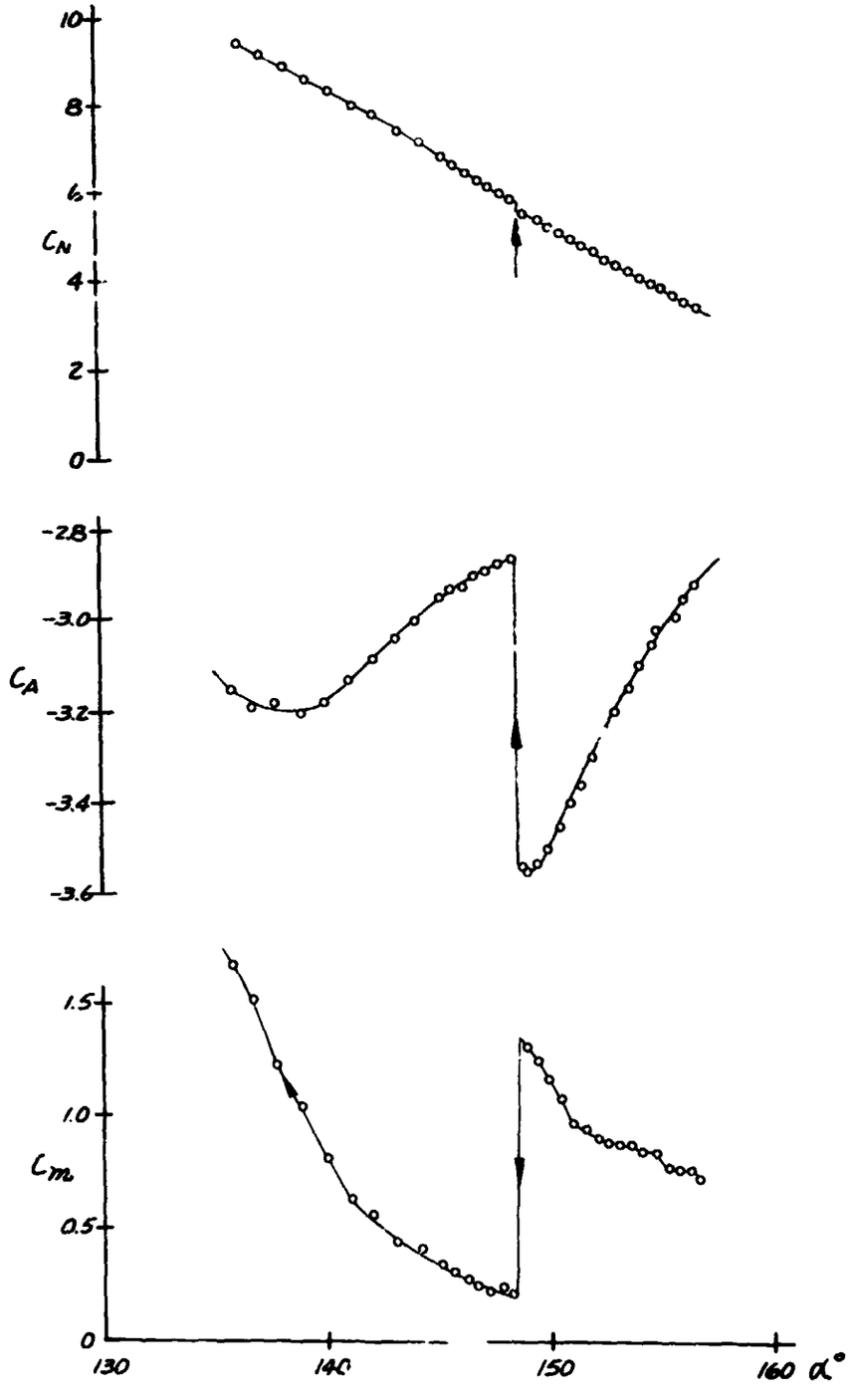

Figure 31 Static Characteristics of the SRM with Nozzle E_{1A} at $M_\infty = 3.48$

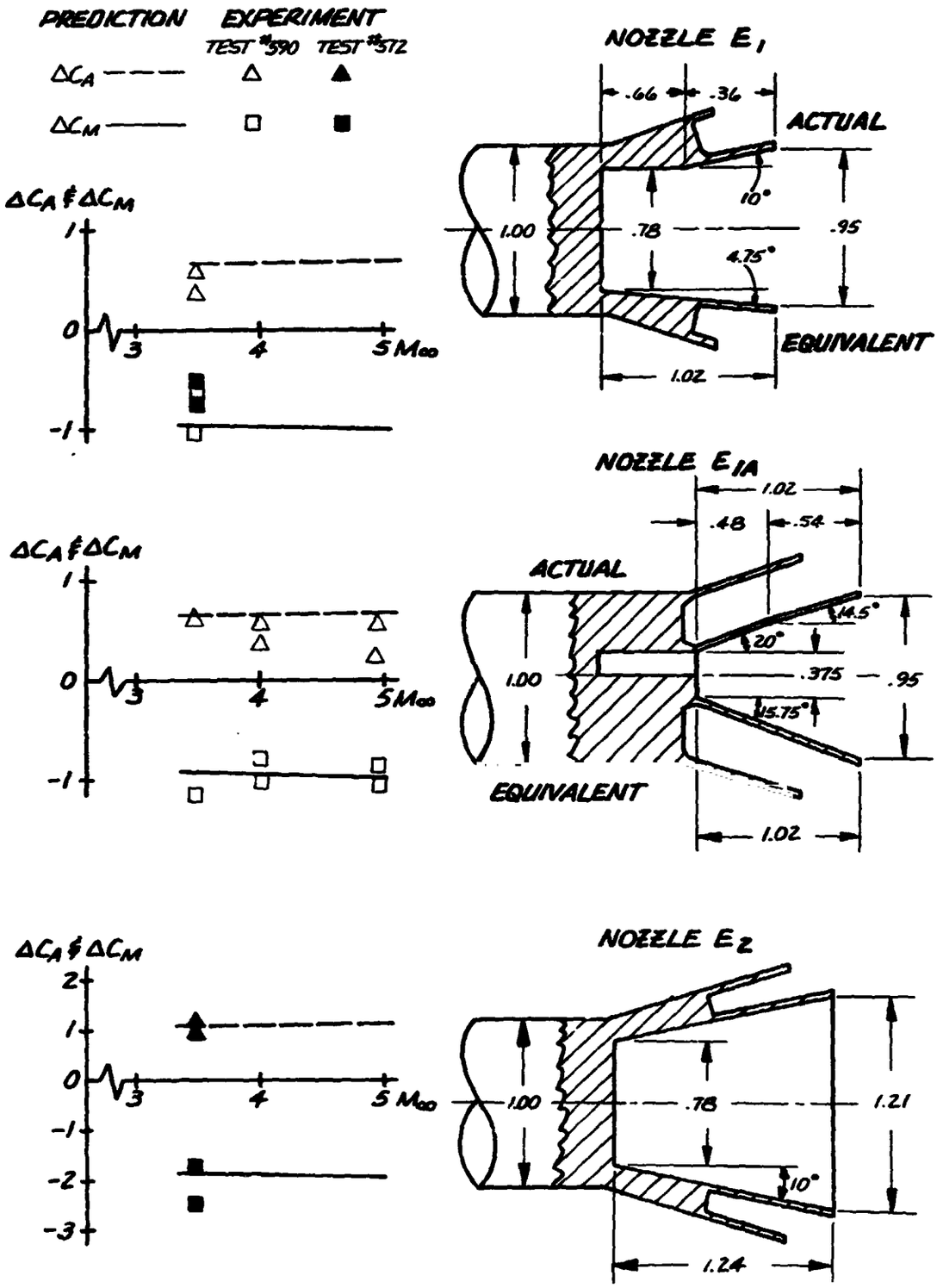

Figure 32 Comparison Between Predicted and Measured Aerodynamic Discontinuities for Three Different Nozzle Geometrics